reflex on the arterial baroreflex.

The performance of the arterial baroreflex system may be evaluated by dynamic and static characteristics [14, 15]. The dynamic characteristics provide information on the speed and stability of the feedback regulation, and the static characteristics provide that on nonlinearity such as threshold and saturation properties. Because the dynamic characteristics are usually determined only around the normal physiological operating point, assessment of the static characteristics are important for understanding the system behavior under pathological conditions where the operating point may be deviated from the center of the system operating range. In short, the dynamic and static characteristics are complementary to each other for fully understanding the system performance.

Because the dynamic characteristics of the arterial baroreflex during the activation of the Bezold-Jarisch reflex were examined in a previous study [16], we focused on the static characteristics in the present study. To identify the static characteristics of the arterial baroreflex over the entire operating range, we performed an open-loop experiment of the carotid sinus baroreflex in anesthetized rabbits. To elucidate how the Bezold-Jarisch reflex affected the system operating point, we used a baroreflex equilibrium diagram composed of neural and peripheral arcs [17]. The neural arc represents the static input-output relationship between baroreceptor pressure input and efferent sympathetic nerve activity, and the peripheral arc represents that between efferent sympathetic nerve activity and AP. The intersection of the neural and peripheral arcs defines the operating point of the AP regulation (see *Theoretical considerations* in MATERIALS AND METHODS for details). Because the previous study indicated that the Bezold-Jarisch reflex attenuated dynamic gain of the baroreflex neural arc [16], we hypothesized that the Bezold-Jarisch reflex would decrease the system operating point by modulating the neural arc characteristics while not significantly affecting the peripheral arc characteristics. The results of the present study indicate that the Bezold-Jarisch reflex markedly shifted the neural arc toward lower sympathetic nerve activity, resulting in the reduction of the system operating point.

MATERIALS AND METHODS

Theoretical considerations. Changes in AP are sensed by the arterial baroreceptors, which alter efferent sympathetic nerve activity via the arterial baroreflex. Changes in efferent sympathetic nerve activity in turn affect AP. This closed-loop nature of the feedback regulation makes it difficult to analyze the behavior of the arterial baroreflex. To circumvent this problem, we opened the feedback loop and divided the arterial baroreflex system into neural and peripheral arcs. In the neural arc, the input is the pressure sensed by the arterial baroreceptors and the output is efferent sympathetic nerve activity. In the peripheral arc, the input is efferent sympathetic nerve activity and the output is AP. Because pressure sensed by the arterial baroreceptors is equilibrated with AP under physiological conditions, we superimposed the functions representing the two arcs in a single diagram and determined the operating point from the intersection of the two arcs. The validity of this framework has been examined in a previous study [17]. The concept of the baroreflex equilibrium diagram was first proposed by Mohrman and Heller and its usefulness in describing many physiological and pathological situations of the circulatory system was well documented in their textbook [18]. Using the baroreflex equilibrium diagram, we aimed to quantify the effects of the Bezold-Jarisch reflex on the carotid sinus baroreflex.

Surgical preparations. Animals were cared for in strict accordance with the *Guiding Principles for the Care and Use of Animals in the Field of Physiological Sciences* approved by the Physiological Society of Japan. Eight Japanese white rabbits weighing 2.6–3.0 kg were anesthetized with an intravenous injection (2 ml/kg) of a mixture of urethane (250 mg/ml) and α-chloralose (40 mg/ml). The rabbits were ventilated artificially with oxygen-enriched room air. To maintain the appropriate level of anesthesia, supplemental doses of these anesthetics were administered continuously (0.2–0.3 ml/kg/h, i.v.). AP was measured using a high-fidelity pressure transducer (Millar Instruments, Houston, TX) inserted from the right femoral artery. A double-lumen catheter was introduced into the right femoral vein for drug administration. To eliminate the effects of the aortic baroreflex, aortic depressor nerves were sectioned after identifying their arterial pulse-synchronous activity. The bilateral vagi were kept intact to preserve the afferent pathway of the cardiopulmonary receptors. We isolated the bilateral carotid sinuses from the systemic circulation by ligating the external and internal carotid arteries and other small branches originating from the carotid sinus regions. The isolated carotid sinuses were filled with warm physiological saline through catheters inserted via the common carotid arteries. Intracarotid sinus pressure (CSP) was controlled by a servo-controlled piston pump driven by a laboratory computer system.

We exposed the left renal sympathetic nerve retroperitoneally and attached a pair of stainless steel wire electrodes (Bioflex wire AS633, Cooner Wire) to record renal sympathetic nerve activity (RSNA). The nerve fibers distal to the electrodes were crushed by tight ligature to eliminate afferent signals from the kidney. To insulate and fix the electrodes and to prevent the nerve from drying, the nerve and the electrodes were covered in silicone gel (Semicosil 932A/B, Wacker Silicones). The preamplified nerve signal, band-pass filtered at 150–1,000 Hz, was full-wave rectified and low-pass filtered with a cutoff frequency of 30 Hz to quantify nerve activity. Pancuronium bromide (0.1 mg/kg, i.v.) was administered to prevent muscular activity from contaminating the RSNA recording. Animal body temperature was kept at around 38°C with a heating pad throughout the experiment. After the experiment, the experimental animal was killed by an overdose of intravenous pentobarbital, and the background noise in the RSNA recording was measured for 1 min under a postmortem state.

Protocol. We evoked the Bezold-Jarish reflex by intravenous administration of phenylbiguanide (PBG), a selective 5-HT_3 receptor agonist, obtained from RBI (Natrick, MA, USA) [19, 20]. A preliminary experiment indicated that acquisition of control data after the cessation of intravenous PBG administration was difficult because of the long-lasting effects of PBG on RSNA, AP, and HR [6]. For this reason, the control data were obtained first in the present study. To evaluate the time effects, we repeated the estimation of the baroreflex static characteristics twice under control conditions (CTL1 and CTL2). The effects of PBG on the baroreflex static characteristics were then examined. In each of the three conditions, CSP was decreased and maintained at 40 mmHg for 4 min until the AP response reached steady state. CSP was then increased every minute from 40 to 160 mmHg in increments of 20 mmHg [21, 22]. For the PBG treatment condition, PBG was administered by a bolus intravenous injection (200 μg/kg) followed by a continuous intravenous infusion (100 $\mu g \cdot kg^{-1} \cdot min^{-1}$) during the experimental period. A preliminary experiment indicated that the effects of PBG with this regimen reached steady state within approximately 3 min.

Data analysis. Data were sampled at 200 Hz using a 12-bit analog-to-digital converter and stored on the hard disk of a dedicated laboratory computer system. To quantify the static characteristics of the carotid sinus baroreflex, we calculated mean RSNA, AP, and HR during the last 10 s of each CSP level. In each animal, RSNA data were presented in arbitrary units (a.u.) so that the background noise level became zero and the RSNA value at the CSP level of 40 mmHg under the CTL1 condition became unity. The static characteristics of the baroreflex total loop (CSP-AP curve), neural arc (CSP-RSNA curve), and baroreflex control of HR (CSP-HR curve) were examined by a regression analysis for the four-parameter logistic function as follows [21–23]:

$$y = \frac{p_1}{1 + \exp[p_2 (x - p_3)]} + p_4 \quad (1)$$

where x and y represent the input and output, respectively. p_1 is the response range (the difference between the maximum and minimum values of y), p_2 is the coefficient of gain, p_3 is the midpoint in the x axis, and p_4 is the minimum value of y.

To quantify static characteristics of the baroreflex peripheral arc, we performed a linear regression analysis on the RSNA-AP data as follows:

$$AP = a \cdot \mathrm{RSNA} + b \quad (2)$$

where a and b represent the peripheral arc gain and offset pressure, respectively.

AP at the system operating point (AP_{OP}) and the open-loop gain of the feedback regulation at the system operating point (G_{OP}) were estimated by the following two methods. In the first method (conventional analysis), AP_{OP} was determined from AP at the intersection point between the fitted logistic function for the CSP-AP data and the line of identity. G_{OP} was then estimated as the slope of the fitted logistic function at CSP = AP_{OP}. In the second method (equilibrium diagram analysis), AP_{OP} was determined from AP at the intersection point between the CSP-RSNA curve and the RSNA-AP line on the baroreflex equilibrium diagram. G_{OP} was then calculated from the product of the CSP-RSNA and RSNA-AP slopes at the operating point [24]. The latter analysis enabled us to determine whether the neural or peripheral arc was mainly responsible for observed changes in AP_{OP} and G_{OP}.

Statistical analysis. The four parameters of the logistic function for the baroreflex total loop, neural arc, and the CSP-HR curve, as well as the two parameters for the baroreflex peripheral arc, were compared among the CTL1, CTL2, and PBG conditions by one-way analysis of variance with repeated measures and the Bonferroni *post hoc* test [25]. AP_{OP} and G_{OP} were also compared among the three conditions by the same statistical procedure. The differences were considered significant at $P < 0.05$.

RESULTS

Figure 1 shows representative recordings of CSP, RSNA, AP, and HR obtained under CTL1, CTL2, and PBG conditions. CSP was increased every minute from 40 to 160 mmHg for each condition. RSNA, AP, and HR were decreased in response to the increments in CSP. There were no significant differences in the RSNA, AP, and HR responses between the CTL1 and CTL2 conditions. PBG treatment markedly decreased RSNA, AP, and HR at each CSP level compared with the CTL1 and CTL2 conditions.

Figure 2A shows static characteristics of the baroreflex total loop under CTL1, CTL2, and PBG conditions averaged from the 8 rabbits. The CSP-AP data had a sigmoidal relationship. The diagonal line indicates the line of identity in each panel. The intersection between the CSP-AP curve and the line of identity corresponds to the closed-loop operating point of the baroreflex negative feedback regulation. The operating point was located in the steepest portion (80–100 mmHg) of the sigmoid curve in the CTL1 and CTL2 conditions. PBG decreased AP at each CSP level compared with the CTL1 and CTL2 conditions. The operating point deviated from the steepest portion to the shallower portion (60–80 mmHg) of the sigmoid curve under the PBG condition.

Table 1 summarizes the regression analysis for the four-parameter logistic function on the CSP-AP data shown in Fig. 2A. The response range, the midpoint of operation, and the minimum AP were significantly smaller in the PBG than in the CTL1 and CTL2 conditions. PBG treatment significantly decreased AP_{OP} and G_{OP} derived from the CSP-AP data compared with the CTL1 and CTL2 conditions.

Figure 2B shows static relationship between CSP and HR under the CTL1, CTL2, and PBG conditions. HR was decreased with increasing CSP under all three conditions. PBG decreased HR at each CSP level compared with the CTL1 and CTL2 conditions.

Table 2 summarizes the regression analysis for the four-parameter logistic function on the CSP-HR data shown in Fig. 2B. The minimum HR was significantly lower in the PBG than in the CTL1 and CTL2 conditions. Other parameters did not differ significantly among the three conditions.

Figure 3A illustrates static characteristics of the baroreflex neural arc averaged from the 8 rabbits. RSNA decreased with increasing CSP under the CTL1, CTL2, and PBG conditions. The relationship between CSP and RSNA approximated a sigmoid curve. PBG moved the sigmoid curve downward. At

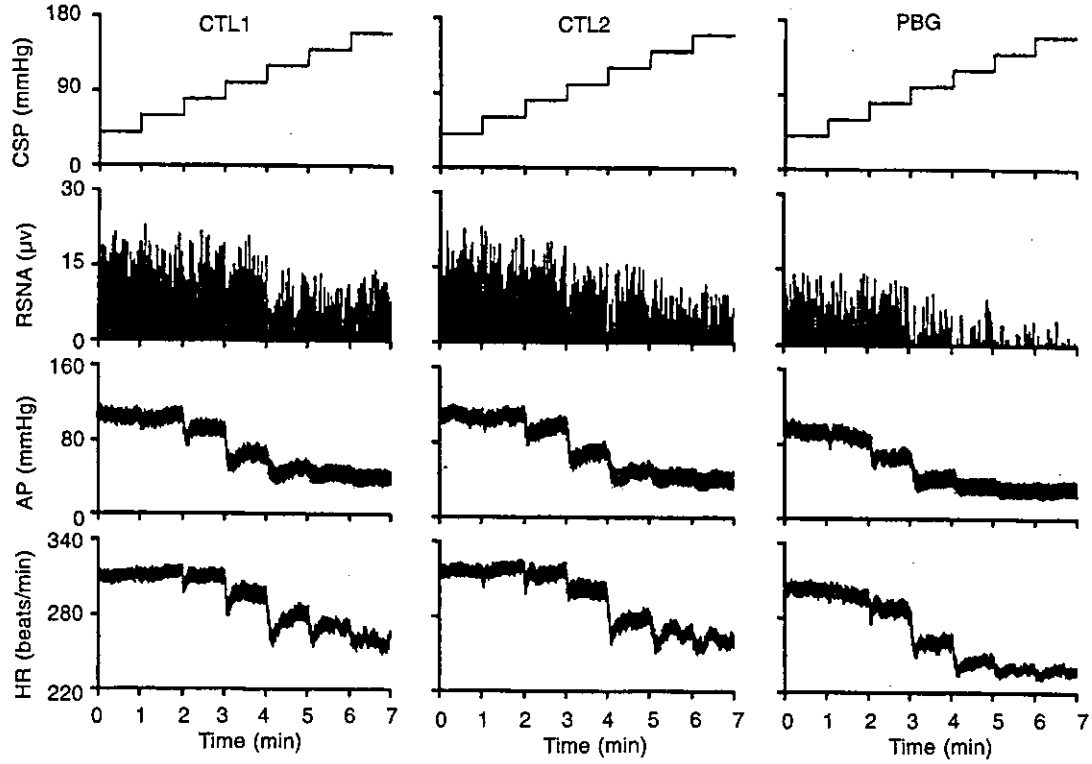

Fig. 1. Typical time series of carotid sinus pressure (CSP), renal sympathetic nerve activity (RSNA), arterial pressure (AP), and heart rate (HR) obtained in the absence (CTL1 and CTL2) and presence of phenylbiguanide (PBG). CSP was increased from 40 to 160 mmHg in 20 mmHg increments, resulting in changes in RSNA, AP, and HR through the carotid sinus baroreflex. Data were resampled at 10 Hz in this figure.

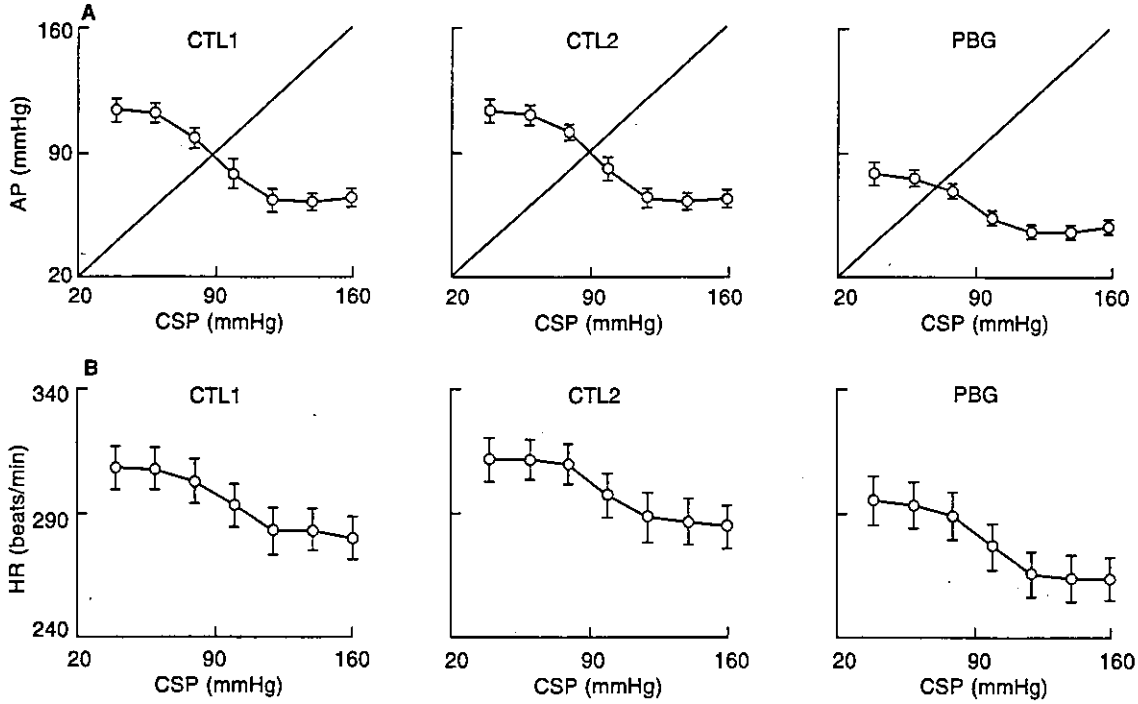

Fig. 2. A: Static characteristics of total baroreflex loop from CSP to AP averaged from all animals under CTL1 (left), CTL2 (middle), and PBG (right) conditions. B: Static characteristics from CSP to HR under CTL1 (left), CTL2 (middle), and PBG (right) conditions. Data are mean ± SEM.

Table 1. Logistic function parameters for the CSP-AP relationship and parameters on the operating point of the baroreflex negative feedback regulation.

	CTL1	CTL2	PBG
Response range, p_1 (mmHg)	54.3 ± 8.4	51.5 ± 8.0	33.6 ± 6.4**††
Coefficient of gain, p_2 (mmHg^{-1})	0.24 ± 0.11	0.34 ± 0.15	0.22 ± 0.10
Midpoint in x axis, p_3 (mmHg)	93.3 ± 3.0	96.2 ± 2.8	86.8 ± 2.0†
Minimum value of y, p_4 (mmHg)	60.9 ± 5.2	61.3 ± 5.0	46.3 ± 2.7**††
AP_{OP} (mmHg)	90.5 ± 3.2	91.3 ± 2.4	71.7 ± 3.1**††
G_{OP}	−1.41 ± 0.40	−1.31 ± 0.44	−0.51 ± 0.14*†

CTL1, CTL2, and PBG represent the conditions of controls and intravenous phenylbiguanide administration. Data are mean ± SEM. **P < 0.01 vs. CTL1. *P < 0.05 vs. CTL1. ††P < 0.01 vs. CTL2. †P < 0.05 vs. CTL2.

Table 2. Logistic function parameters for the CSP-HR relationship.

	CTL1	CTL2	PBG
Response range, p_1 (beats/min)	30.2 ± 7.7	27.7 ± 7.5	33.8 ± 7.5
Coefficient of gain, p_2 (mmHg^{-1})	0.22 ± 0.12	0.28 ± 0.12	0.40 ± 0.16
Midpoint in x axis, p_3 (mmHg)	103.0 ± 4.5	102.8 ± 3.7	98.4 ± 4.5
Minimum value of y, p_4 (beats/min)	278.9 ± 9.2	284.7 ± 9.3	262.5 ± 8.9*††

CTL1, CTL2, and PBG represent the conditions of controls and intravenous phenylbiguanide administration. Data are mean ± SEM. *P < 0.05 vs. CTL1. ††P < 0.01 vs. CTL2.

the CSP level of 40 mmHg, RSNA was decreased to approximately 60% by the PBG treatment.

Figure 3B illustrates static characteristics of the baroreflex peripheral arc averaged from the 8 rabbits. AP increased with increasing RSNA under the CTL1, CTL2, and PBG conditions. The relationship between RSNA and AP approximated a straight line in each panel. The slope of the line or the peripheral arc gain was slightly smaller in the PBG than in the CTL1 and CTL2 conditions.

Table 3 summarizes the regression analyses for the baroreflex neural and peripheral arcs. In the neural arc, the response range and the coefficient of gain in the PBG condition did not differ from those in the CTL1 and CTL2 conditions, suggesting a parallel shift in the CSP-RSNA curve. PBG lowered the midpoint

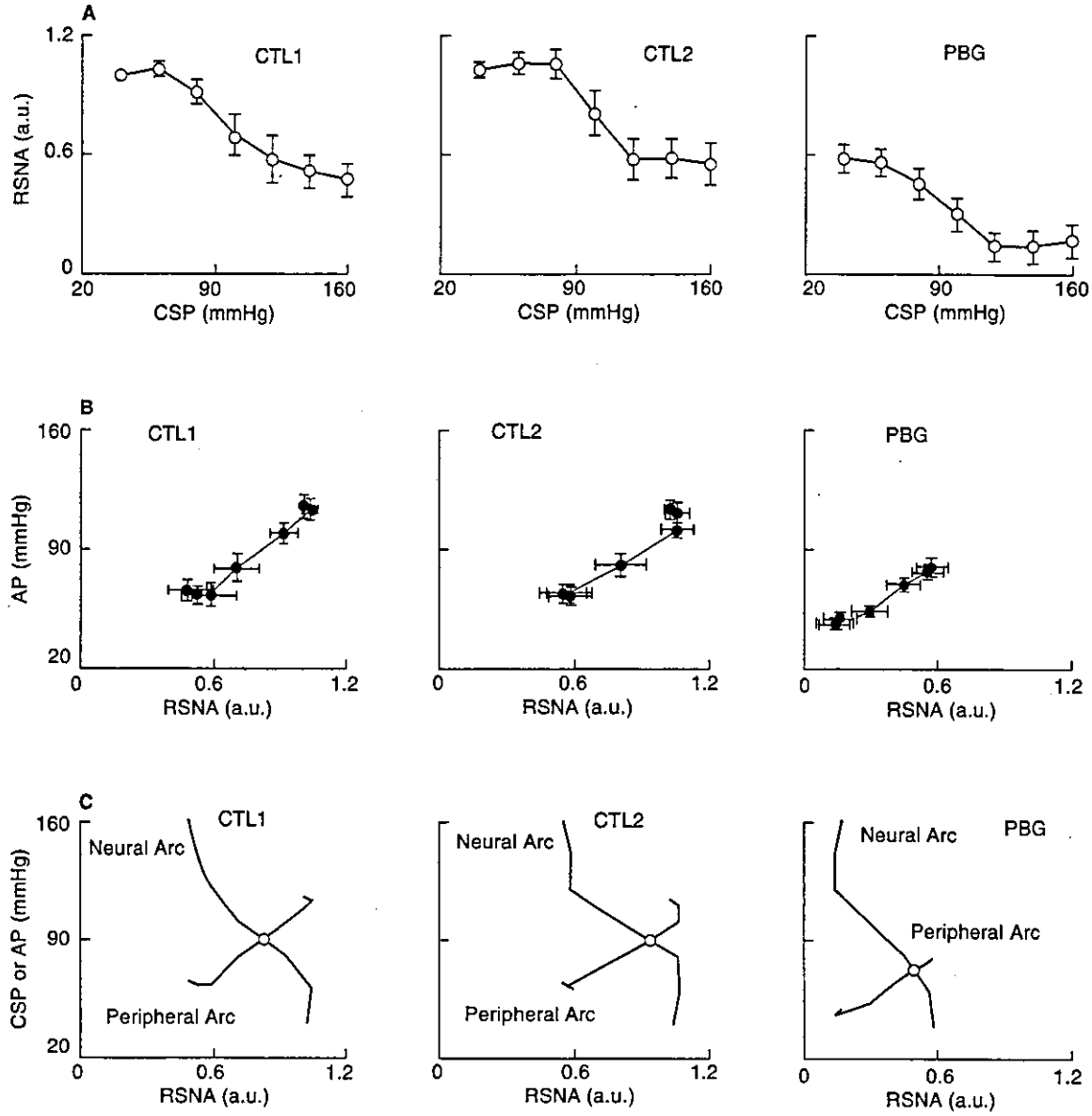

Fig. 3. A: Static characteristics of the neural arc from CSP to RSNA averaged from all animals under CTL1 (left), CTL2 (middle), and PBG (right) conditions. B: Static characteristics from RSNA to AP under CTL1 (left), CTL2 (middle), and PBG (right) conditions. C: Equilibrium diagrams between the neural and peripheral arcs before (CTL1 and CTL2; left and middle) and after PBG administration (right). Data are mean ± SEM. Open circle represents the closed-loop operating point of the baroreflex negative feedback regulation.

Table 3. Logistic function parameters of the neural arc from CSP to RSNA and linear regression parameters of the peripheral arc from RSNA to AP.

	CTL1	CTL2	PBG
Neural arc			
Response range, p_1 (a.u.)	0.55 ± 0.09	0.52 ± 0.10	0.47 ± 0.06
Coefficient of gain, p_2 ($mmHg^{-1}$)	0.34 ± 0.13	0.53 ± 0.16	0.32 ± 0.14
Midpoint in x axis, p_3 (mmHg)	99.1 ± 5.7	102.0 ± 3.9	89.6 ± 2.6†
Minimum value of y, p_4 (a.u.)	0.47 ± 0.09	0.53 ± 0.10	0.12 ± 0.07**††
Peripheral arc			
Gain (mmHg/a.u.)	94.1 ± 12.6	91.8 ± 12.5	67.4 ± 8.0**†
Offset pressure (mmHg)	15.1 ± 8.5	14.6 ± 6.7	38.2 ± 3.6**††
AP_{OP}	89.9 ± 4.0	95.1 ± 3.2	70.8 ± 3.1**††
G_{OP}	−1.64 ± 0.44	−1.52 ± 0.56	−0.52 ± 0.21*†

Data are mean ± SEM. **P < 0.01 vs. CTL1. ††P < 0.01 vs. CTL2. *P < 0.05 vs. CTL1. †P < 0.05 vs. CTL2.

of operation and minimum RSNA compared with the CTL1 and CTL2 conditions. In the peripheral arc, the peripheral arc gain was significantly smaller whereas the offset pressure was significantly greater in the PBG than in the CTL1 and CTL2 conditions.

Figure 3C depicts the baroreflex equilibrium diagram obtained from the averaged data points shown in Fig. 3, A and B. The intersection between the neural and peripheral arcs provides the closed-loop operating point of the baroreflex negative feedback regulation (open circles). PBG markedly shifted the baroreflex neural arc toward lower RSNA and slightly decreased the peripheral arc gain. AP_{OP} and G_{OP} derived from the equilibrium diagram (Table 3) were close to those derived from the CSP-AP data (Table 1). Here, the G_{OP} in Table 3 was determined by the product of the neural arc gain and the peripheral arc gain at the operating point. When compared with the averaged value obtained from CTL1 and CTL2 conditions, PBG decreased the neural arc gain to 42.5 ± 16.0% and the peripheral arc gain to 76.9 ± 7.3% at the operating point.

DISCUSSION

The Bezold-Jarisch reflex evoked by intravenous PBG administration exerted inhibitory effects on RSNA, AP, and HR. We have shown, using the baroreflex equilibrium diagram analysis, that the reduction of AP_{OP} and G_{OP} was mainly attributable to the shift in the neural arc toward lower RSNA.

Effects of PBG on baroreflex static characteristics. Intravenous administration of PBG shifted the CSP-AP curve downward and attenuated the response range of AP (Fig. 2A). Because the CSP-AP curves did not differ between CTL1 and CTL2, the observed changes in the CSP-AP curve during PBG treatment were not resulting from the cumulative effects of continuous administration of anesthetics or from the time-dependent deterioration of the preparation. Changes in the CSP-AP curve were consistent with those reported by Chen [7] where the effects of intravenous veratridine administration on the CSP-AP curve were examined in anesthetized rabbits. Chen also demonstrated that veratridine depressed the CSP-HR curve downward and the depression of HR was more prominent at lower CSP levels. In contrast, the response range of HR did not change significantly despite the marked downward shift of the CSP-HR curve in the present study (Fig. 2B). The minimum HR under the control conditions was approximately 180 beats/min in the study by Chen, whereas it was approximately 280 beats/min in the present study, suggesting a marked difference in the background autonomic tone. Although the exact cause for the different autonomic tone is unclear, the HR decreasing effect of the Bezold-Jarisch reflex might have been saturated in his study due to lower HR under the control conditions.

To elucidate the mechanism for the CSP-AP curve depression by the Bezold-Jarisch reflex, we constructed a baroreflex equilibrium diagram by superimposing the CSP-RSNA and RSNA-AP curves (Fig. 3C). AP_{OP} and G_{OP} derived from the equilibrium diagram matched with those estimated from CSP-AP data (Tables 1 and 3), suggesting reasonable accuracy of the equilibrium diagram analysis. Intravenous PBG shifted the CSP-RSNA curve toward lower RSNA, resulting in the decreased AP_{OP}. The decrease in AP_{OP} reduced the neural arc gain to approximately 43% and the peripheral arc gain to approximately 77% at the operating point. Therefore, changes in the neural arc gain contributed to the reduction of G_{OP} much more than changes in the peripheral arc gain.

Previous studies indicated that the Bezold-Jarisch reflex might interfere with the baroreflex signal transduction in such brainstem areas as the nucleus tractus solitarius (NTS) and the rostral ventrolateral medulla (RVLM). Merahi *et al.* [26] demonstrated that most 5-HT_3 receptors in the NTS were found on the vagal sensory afferent fibers. Pires *et al.* [27] reported that the NTS was involved in the central pathways of the Bezold-Jarisch reflex. Verberne *et al.* [8] demonstrated that barosensitive neurons in the RVLM were inhibited by intravenous injection of PBG. In the present study, however, the response range of RSNA to the CSP input was well maintained in spite of the significant decrease in RSNA (Fig. 3A, Table 3). Therefore, some barosensitive neurons appear to be independent of the Bezold-Jarisch reflex.

In the peripheral arc static characteristics, AP was significantly higher at lower RSNA levels, making the offset pressure higher and the peripheral arc gain smaller (Fig. 3B, Table 3). Borovikova *et al.* [28] reported that direct electrical stimulation of the peripheral efferent vagus during lethal endotoxic shock inhibited tumor necrosis factor (TNF) synthesis in the liver and inhibited progress in hypotension in rats. Guarini *et al.* [29] reported that efferent vagal stimulation during hypovolemic hemorrhagic shock attenuated TNF-α and nuclear factor κB (NF-κB) in the liver and inhibited severe hypotension in rats. In the present study, because we depicted changes in AP as a function of RSNA in the peripheral arc, any influence on AP independent of RSNA caused apparent changes in the peripheral arc. We think that the

Bezold-Jarisch reflex increased vagal efferent activity, which might have elevated AP at lower RSNA levels via the anti-inflammatory mechanism. Regional difference in sympathetic nerve activation may also account for the changes in the peripheral arc. If the Bezold-Jarisch reflex alters regional distribution of sympathetic drives among organs compared with the control conditions, it would result in changes in the RSNA-AP relationship. Further studies are required to clarify whether the Bezold-Jarisch reflex affects regional distribution of sympathetic drives.

Clinical implications. Figure 4 illustrates a putative baroreflex equilibrium diagram explaining the effects of the Bezold-Jarisch reflex on the AP regulation. As discussed in the previous section, the neural arc and peripheral arc intersect near the steepest portion of the neural arc under control conditions (point "a"). Because the Bezold-Jarisch reflex shifts the neural arc toward lower RSNA, the two arcs intersect at the shallower portion of the neural arc (point "b"). Although the peripheral arc gain decreased only to 77% during PBG treatment in the present study, it could be much lower in acute myocardial ischemia or infarction because of the pump failure of the heart (dashed line). The shift in the peripheral arc during pump failure would move the operating point to a region where the neural arc hardly responds to changes in CSP (point "c"). In other words, G_{OP} might approach zero under acute myocardial ischemia or infarction. Under such conditions, the exogenous pressure disturbance directly affects AP without any buffering via the baroreflex regulation.

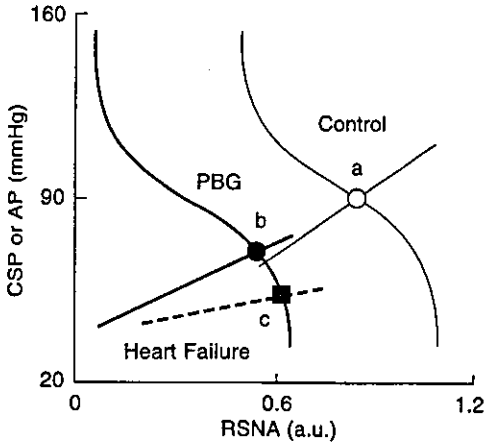

Fig. 4. Putative diagram of the arterial baroreflex controls of RSNA and AP during the Bezold-Jarisch reflex. The operating point of the baroreflex negative feedback regulation is at the steepest portion of the neural arc under the control conditions (point "a"). The Bezold-Jaricsh reflex induced by phenylbiguanide moves the operating point to point "b," reducing AP and total loop gain at the operating point. Under myocardial ischemia or infarction, the peripheral arc gain could decrease due to pump failure (dashed line), which moves the operating point to lower AP (point "c") where the neural arc hardly responds to changes in CSP.

The Bezold-Jarisch reflex could prevent overexertion of cardiac muscle by bradycardia and hypotension [13]. The reduction of energy consumption may be beneficial for reducing ischemic insult and salvaging tissues in the ischemic border zone. However, the Bezold-Jarisch reflex attenuates the performance of the arterial baroreflex. Once the hypotension exceeds a critical level, no buffering effects via the native baroreflex regulation would be expected. Therefore, excess activation of the Bezold-Jarisch reflex could lead to severe bradycardia and hypotension, placing the patient's life at risk. Because the magnitude of the Bezold-Jarisch reflex was not investigated in the present study, future experiments should focus on the magnitude of the Bezold-Jarisch reflex using models of actual myocardial ischemia or infarction such as that induced by the coronary artery occlusion.

Limitations. There are several limitations to this study. First, as the anesthesia affects autonomic nerve activities [30], the results might have been different had we performed the experiment with other anesthetic conditions or without anesthetics.

Second, the surgical isolation of the carotid sinuses might damage the baroreceptors and carotid sinus nerves to varying degrees. The carotid sinus baroreflex alone did not suppress RSNA completely under control conditions in the present study, and therefore there was a margin for decreasing the minimum RSNA during the PBG condition. If the minimum RSNA reached the noise level at higher CSP levels under control conditions, however, PBG treatment could not further suppress RSNA, inevitably reducing the response range of RSNA. We speculate that the integration of the carotid sinus baroreflex and the Bezold-Jarisch reflex in determining RSNA depends on the magnitude of RSNA inhibition induced by the respective reflexes. Such a nonlinear summation, dependent on the size of input signals, is also found between carotid sinus and aortic arch baroreflexes [15].

Third, intravenous PBG administration could have direct effects on the baroreflex neural and peripheral characteristics. However, vagotomy eliminated the inhibitory effects of PBG on RSNA and AP in our previous study using similar experimental settings [16]. Therefore, changes in baroreflex controls of RSNA and AP during PBG treatment were most likely mediated by the activation of vagal afferent fibers. With respect to HR, intravenous PBG administration

slightly increased HR under the vagotomized condition. The CSP-HR curve shown in Fig. 2B might therefore be modulated to some extent by the direct action of PBG on HR.

In conclusion, the reduction of AP_{OP} and G_{OP} during the Bezold-Jarisch reflex was mainly due to the shift of static characteristics in the neural arc toward lower RSNA. Although the Bezold-Jarisch reflex decreased G_{OP} to approximately 35% in the present study (Tables 1 and 3), G_{OP} could approach zero during acute myocardial ischemia or infarction because of the reduced peripheral arc gain and further decrease in AP_{OP} (Fig. 4). Therefore, preventing severe hypotension during the activation of the Bezold-Jarisch reflex associated with acute myocardial ischemia or infarction would be essential for increasing AP stability via the native baroreflex system.

This study was supported by Health and Labour Sciences Research Grant for Research on Advanced Medical Technology from the Ministry of Health Labour and Welfare of Japan (13090401, H14-Nano-002), by Grant-in-Aid for Scientific Research (A:15200040, C:15590786) from the Japan Society for the Promotion of Science, and by the Program for Promotion of Fundamental Studies in Health Science of the Organization for Pharmaceutical Safety and Research of Japan.

REFERENCES

1. Aviado DM, and Aviado DG: The Bezold-Jarisch reflex. A historical perspective of cardiopulmonary reflexes. Ann NY Acad Sci 940: 48–58, 2001
2. Hainsworth R: Reflexes from the heart. Physiol Rev 71: 617–658, 1991
3. Bezold A, and Hirt L: Uber die physiologischen Wirkungen des essingsauren Veratrins. Unters Physiol Lab Wurtzburg 1: 75–156, 1867
4. Jarisch A, and Richter H: Die afferenten Bahnen des Veratrineeffekts in den Herznerven. Arch Exp Pathol Pharmakol 193: 355–371, 1939
5. Veelken R, Hilgers KF, Leonard M, Scrogin K, Ruhe J, Mann JF, and Luft FC: A highly selective cardiorenal serotonergic 5-HT3-mediated reflex in rats. Am J Physiol 264: H1871–H1877, 1993
6. Veelken R, Leonard M, Stetter A, Hilgers KF, Mann JF, Reeh PW, Geiger H, and Luft FC: Pulmonary serotonin 5-HT3-sensitive afferent fibers modulate renal sympathetic nerve activity in rats: Am J Physiol 272: H979–H986, 1997
7. Chen HI. Interaction between the baroreceptor and Bezold-Jarisch reflexes: Am J Physiol Heart Circ Physiol 237: H655–H661, 1979
8. Verberne AJ, and Guyenet PG. Medullary pathway of the Bezold-Jarisch reflex in the rat: Am J Physiol Regulatory Integrative Comp Physiol 263: R1195–R1202, 1992
9. Whalen EJ, Johnson AK, and Lewis SJ. Functional evidence for the rapid desensitization of 5-HT3 receptors on vagal afferents mediating the Bezold-Jarisch reflex: Brain Res 873: 302–305, 2000
10. Meyrelles SS, Bernardes CF, Modolo RP, Mill JG, and Vasquez EC: Bezold-Jarisch reflex in myocardial infarcted rats. J Auton Nerv Syst 63: 144–152, 1997
11. Robertson D, Hollister AS, Forman MB, and Robertson RM: Reflexes unique to myocardial ischemia and infarction. J Am Coll Cardiol 5: 99B–104B, 1985
12. Mark AL: The Bezold-Jarisch reflex revisited: clinical implications of inhibitory reflexes originating in the heart. J Am Coll Cardiol 1: 90–102, 1983
13. Schultz HD: Cardiac vagal chemosensory afferents. Function in pathophysiological states. Ann NY Acad Sci 940: 59–73, 2001
14. Ikeda Y, Kawada T, Sugimachi M, Kawaguchi O, Shishido T, Sato T, Miyano H, Matsuura W, Alexander J Jr, and Sunagawa K: Neural arc of baroreflex optimizes dynamic pressure regulation in achieving both stability and quickness. Am J Physiol Heart Circ Physiol 271: H882–H890, 1996
15. Yamazaki T, and Sagawa K: Summation of sinoaortic baroreflexes depends on size of input signals. Am J Physiol 257: H465–H472, 1989
16. Kashihara K, Kawada T, Yanagiya Y, Uemura K, Inagaki M, Takaki H, Sugimachi M, and Sunagawa K: Bezold-Jarisch reflex attenuates dynamic gain of baroreflex neural arc. Am J Physiol Heart Circ Physiol 285: H833–H840, 2003
17. Sato T, Kawada T, Inagaki M, Shishido T, Takaki H, Sugimachi M, and Sunagawa K: New analytic framework for understanding the sympathetic baroreflex control of arterial pressure. Am J Physiol Heart Circ Phisiol 276: H2251–H2261, 1999
18. Mohrman DE, and Heller LJ: Cardiovascular Physiology, 4th ed, pp 151–173, McGraw-Hill, New York, 1997
19. Hardcastle J, and Hardcastle PT: 5-Hydroxytryptamine-induced secretion by rat jejunum *in-vitro* involves several 5-hydroxytryptamine receptor subtypes. J Pharm Pharmacol 50: 539–547, 1998
20. Mair ID, Lambert JJ, Yang J, Dempster J, and Peters JA: Pharmacological characterization of a rat 5-hydroxytryptamine type3 receptor subunit (r5-HT3A(b)) expressed in Xenopus laevis oocytes. Br J Pharmacol 124: 1667–1674, 1998
21. Kawada T, Shishido T, Inagaki M, Tatewaki T, Zheng C, Yanagiya Y, Sugimachi M, and Sunagawa K: Differential dynamic baroreflex regulation of cardiac and renal sympathetic nerve activities. Am J Physiol Heart Circ Physiol 280: H1581–H1590, 2001
22. Sato T, Kawada T, Miyano H, Shishido T, Inagaki M, Yoshimura R, Tatewaki T, Sugimachi M, Alexander J Jr, and Sunagawa K: New simple methods for isolating baroreceptor regions of carotid sinus and aortic depressor nerves in rats. Am J Physiol 276: H326–H332, 1999
23. Kent BB, Drane JW, Blumenstein B, and Manning JW: A mathematical model to assess changes in the baroreceptor reflex. Cardiology 57: 295–310, 1972
24. Kawada T, Shishido T, Inagaki M, Zheng C, Yanagiya Y, Uemura K, Sugimachi M, and Sunagawa K: Estimation of baroreflex gain using a baroreflex equilibrium diagram. Jpn J Physiol 52: 21–29, 2002
25. Glantz SA: Primer of Biostatistics, 4th ed, McGraw Hill, New York, 1997

26. Merahi N, Orer HS, Laporte AM, Gozlan H, Hamon M, and Laguzzi R: Baroreceptor reflex inhibition induced by the stimulation of serotonin$_3$ receptors in the nucleus tractus solitarius of the rat. Neuroscience 46: 91–100, 1992
27. Pires JG, Silva SR, Ramage AG, and Futuro-Neto HA: Evidence that 5-HT3 receptors in the nucleus tractus solitarius and other brainstem areas modulate the vagal bradycardia evoked by activation of the von Bezold-Jarisch reflex in the anesthetized rat. Brain Res 791: 229–234, 1998
28. Borovikova LV, Ivanova S, Zhang M, Yang H, Botchkina GI, Watkins LR, Wang H, Abumrad N, Eaton JW, and Tracey KJ: Vagus nerve stimulation attenuates the systemic inflammatory response to endotoxin. Nature 405: 458–462, 2000
29. Guarini S, Altavilla D, Cainazzo MM, Giuliani D, Bigiani A, Marini H, Squadrito G, Minutoli L, Bertolini A, Marini R, Adamo EB, Venuti FS, and Squadrito F: Efferent vagal fibre stimulation blunts nuclear factor-κB activation and protects against hypovolemic hemorrhagic shock. Circulation 107: 1189–1194, 2003
30. Suzuki S, Ando S, Imaizumi T, and Takeshita A: Effects of anesthesia on sympathetic nerve rhythm: power spectral analysis. J Auton Nerv Syst 43: 51–58, 1993

Am J Physiol Heart Circ Physiol 287: H2906–H2913, 2004;
doi:10.1152/ajpheart.00035.2004.

A self-calibrating telemetry system for measurement of ventricular pressure-volume relations in conscious, freely moving rats

Kazunori Uemura,[1] Toru Kawada,[1] Masaru Sugimachi,[1] Can Zheng,[1,2,3] Koji Kashihara,[1,3] Takayuki Sato,[4] and Kenji Sunagawa[1]

[1]*Department of Cardiovascular Dynamics, National Cardiovascular Center Research Institute, Suita 565-8565;* [2]*Japan Space Forum, Tokyo 105-0013;* [3]*Organization of Pharmaceutical Safety and Research, Tokyo 100-0013; and* [4]*Department of Cardiovascular Control, Kochi Medical School, Nankoku 783-8505, Japan*

Submitted 15 January 2004; accepted in final form 28 July 2004

Uemura, Kazunori, Toru Kawada, Masaru Sugimachi, Can Zheng, Koji Kashihara, Takayuki Sato, and Kenji Sunagawa. A self-calibrating telemetry system for measurement of ventricular pressure-volume relations in conscious, freely moving rats. *Am J Physiol Heart Circ Physiol* 287: H2906–H2913, 2004; doi:10.1152/ajpheart.00035.2004.—Using Bluetooth wireless technology, we developed an implantable telemetry system for measurement of the left ventricular pressure-volume relation in conscious, freely moving rats. The telemetry system consisted of a pressure-conductance catheter (1.8-Fr) connected to a small (14-g) fully implantable signal transmitter. To make the system fully telemetric, calibrations such as blood resistivity and parallel conductance were also conducted telemetrically. To estimate blood resistivity, we used four electrodes arranged 0.2 mm apart on the pressure-conductance catheter. To estimate parallel conductance, we used a dual-frequency method. We examined the accuracy of calibrations, stroke volume (SV) measurements, and the reproducibility of the telemetry. The blood resistivity estimated telemetrically agreed with that measured using an ex vivo cuvette method ($y = 1.09x - 11.9$, $r^2 = 0.88$, $n = 10$). Parallel conductance estimated by the dual-frequency (2 and 20 kHz) method correlated well with that measured by a conventional saline injection method ($y = 1.59x - 1.77$, $r^2 = 0.87$, $n = 13$). The telemetric SV closely correlated with the flowmetric SV during inferior vena cava occlusions ($y = 0.96x + 7.5$, $r^2 = 0.96$, $n = 4$). In six conscious rats, differences between the repeated telemetries on different days (3 days apart on average) were reasonably small: 13% for end-diastolic volume, 20% for end-systolic volume, 28% for end-diastolic pressure, and 6% for end-systolic pressure. We conclude that the developed telemetry system enables us to estimate the pressure-volume relation with reasonable accuracy and reproducibility in conscious, untethered rats.

conductance catheter; serial reproducibility; volumetric accuracy; dual-frequency method; Bluetooth

SMALL EXPERIMENTAL ANIMALS, such as rats and mice, are widely used in cardiovascular research. These animals can offer a variety of disease models, including heart failure and hypertension, and enable us to analyze the molecular mechanisms of the pathophysiology underlying such diseases (5, 7, 12, 21, 27). To interpret the molecular findings in terms of cardiac phenotype, an accurate assessment of cardiac function, including the contractile properties of the left ventricle (LV), is required. As a load-insensitive index of LV contractility, the end-systolic pressure-volume relation (ESPVR) has been estimated in small animal species with the use of a conductance catheter technique or an ultrasonic crystal method in acute experimental settings (6, 9, 14, 15, 23). However, the anesthesia and thoracotomy required by these techniques inevitably exert adverse effects on the heart (13, 22, 30). In addition, the time course of disease progression or long-term drug effects cannot be assessed in acute experimental settings (7, 16). To overcome these problems, long-term experimental settings should be developed where the LV pressure-volume relation can be measured telemetrically in small experimental animals.

In the present study, we have developed a new telemetry system to measure LV volume, pressure, and electrocardiogram (ECG) in conscious, freely moving rats. In this system, the LV pressure-volume relation was obtained from a pressure-conductance catheter chronically implanted in the rat LV. To calibrate the conductance signal and obtain absolute LV volume, measurements of blood resistivity (ρ) and parallel conductance (G_p) are required (3, 4). These calibration procedures require blood sampling and hypertonic saline infusion, but such ex vivo procedures are not applicable to conscious, freely moving small animals. To circumvent such ex vivo procedures in our new telemetry system (29), we adopted a self-calibrating method for the LV volume measurement, as reported in our previous study (28). The aim of the present study was therefore to develop a telemetry system and evaluate its performance. Our results indicate that we succeeded in measuring the LV pressure-volume relation in conscious, untethered rats with reasonable accuracy and reproducibility.

METHODS

Implantable Pressure-Volume Telemetry System

Figure 1*A* illustrates a newly developed pressure-volume telemetry system for rats; it consists of a pressure-conductance catheter, an analog processor-transmitter (weight = 14 g, volume = 11 ml), and a battery unit (lithium battery; weight = 12 g, volume = 10 ml).

Pressure-conductance catheter. Details of the pressure-conductance catheter are presented in Fig. 1*B*. To measure LV conductance, four platinum electrodes (0.25 mm wide) were used. Constant excitation current was applied to the two outermost electrodes while the voltage signal associated with LV conductance was measured from the two inner sensing electrodes. To measure LV pressure, a high-fidelity pressure transducer (Millar Instruments, Houston, TX) was mounted between the two sensing electrodes for the LV conductance measurement. To measure ρ, four smaller platinum electrodes (0.1 mm wide, 0.2 mm between centers of adjacent electrodes, 0.6 mm

Address for reprint requests and other correspondence: K. Uemura, Dept. of Cardiovascular Dynamics, National Cardiovascular Center Research Institute, 5-7-1, Fujishirodai, Suita 565-8565, Japan (E-mail: kuemura@ri.ncvc.go.jp).

The costs of publication of this article were defrayed in part by the payment of page charges. The article must therefore be hereby marked "*advertisement*" in accordance with 18 U.S.C. Section 1734 solely to indicate this fact.

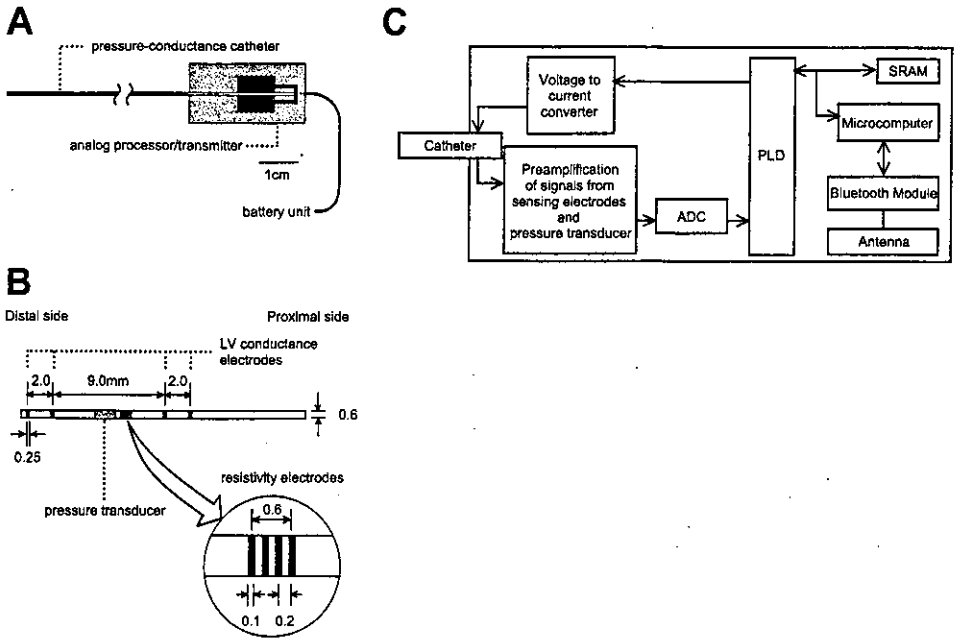

Fig. 1. *A*: schematic illustration of our pressure-volume telemetry system. A 10-cm-long pressure-conductance catheter obtains signals of left ventricular (LV) conductance and pressure, intraventricular blood resistivity, and an ECG. Signals are processed and transmitted by an analog processor transmitter, which is powered by a battery unit (lithium battery). *B*: schematic illustration of our pressure-conductance catheter. Catheter has 4 electrodes for measurement of LV conductance and 4 electrodes for measurement of intraventricular blood resistivity (*inset*). A high-fidelity pressure transducer is mounted between *electrodes 2* and *3*. *C*: block diagram of an analog processor transmitter. ADC, analog-to-digital converter; PLD, programmable logic device; SRAM, static random access memory.

between centers of excitation electrodes) were placed near the pressure transducer (Fig. 1*B*, *inset*). Constant excitation current was applied to the two outer electrodes while the voltage signal associated with ρ was measured from the two inner electrodes.

Analog processor transmitter. A block diagram of the analog processor transmitter is presented in Fig. 1*C*. It was equipped with several functions. First, it delivered a dual-frequency (2 and 20 kHz) constant excitation current [20 μA root mean square (RMS)] for measurements of LV conductance and ρ. We validated the current output by injecting it into known resistors and examining the developed voltage. The resulting RMS current output was 20.4 μA (SD 0.2) and 19.3 μA (SD 0.2) at 2 and 20 kHz, respectively. These values were constant over different resistors (50–990 Ω). Second, it measured and processed the voltage signal from the sensing electrodes as follows: Analog signals were digitized (12 bits, 40-kHz sampling rate; model ADS7870, Texas Instruments, Dallas, TX) and then fed into a programmable logic device (model XC 2C256, Xilinx, San Jose, CA), which processed them to yield RMS digital signals corresponding to frequency components of 2 and 20 kHz and a low-frequency signal (<2 kHz; see APPENDIX). The circuit was connected to the larger or smaller electrodes in response to a command signal, so that LV conductance or ρ could be measured. Third, the analog processor-transmitter had a bridge amplifier for the LV pressure measurement. The LV pressure signal was also digitized (12 bits, 40-kHz sampling rate). All these functions were controlled by a microcomputer (model H8S, Hitachi, Tokyo, Japan).

Bluetooth technology was used to transmit the data (18). For real-time monitoring, all processed signals were resampled at 200 Hz by the microcomputer and transmitted to an external receiver (CASIRA, CSR, Cambridge, UK) by a Bluetooth module (model LMBTB027, Murata, Tokyo, Japan). For high-precision non-real-time analysis, signals recorded at 2,000 Hz over a 6-s interval were stored in a static random access memory (model HM62V16256, Hitachi) and then transmitted to the receiver by the Bluetooth module. The external receiver detected the radio-frequency signal from the transmitter and converted it to a serial bit stream.

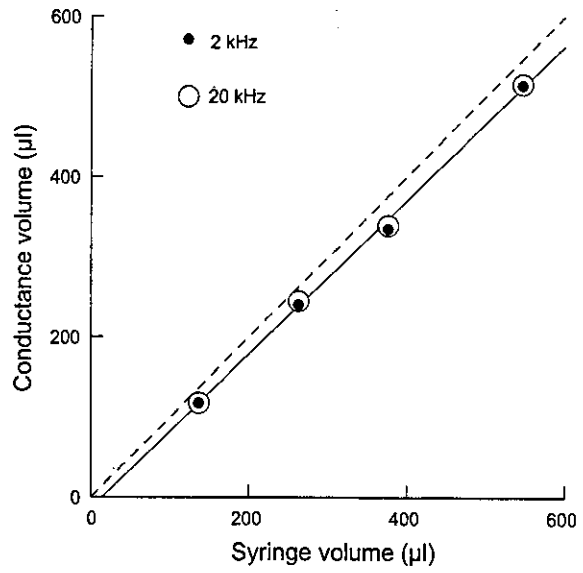

Fig. 2. Comparison of conductance-derived volumes at 2 and 20 kHz vs. known fluid volumes of syringes. Both conductance-derived volumes were essentially identical for each of the syringe volumes. Relation between conductance-derived volume and syringe volume was quite linear. Solid line, regression between conductance-derived volume at 20 kHz and syringe volume; dashed line, identity.

Self-Calibration of Ventricular Volumetry

The principles of conductance volumetry have been described previously (3, 4). Briefly, the ventricular conductance signal (G) can be converted to absolute ventricular volume (V) as follows

$$V = (1/\alpha)\,(L^2 \cdot \rho)\,(G - G_p) \qquad (1)$$

where α is a volume calibration factor, L is the distance between the sensing electrodes, ρ is blood resistivity, and G_p is parallel conductance. L was 9 mm in the present catheter design.

In a preliminary experiment, when the catheter was placed in a series of graduated syringes filled with diluted saline, conductance-derived volumes at 2 and 20 kHz were close to the true syringe volume in the volume range of interest (Fig. 2). Conductance-derived volumes at the two frequencies were essentially identical for each of the syringe volumes. Hence, α was assumed to be unity in the present study (14, 23).

The four smaller electrodes were used to estimate ρ (Fig. 1*B*, *inset*). The distance between the excitation electrodes was set at 0.6 mm. In an in vitro experiment, we confirmed that the current distribution volume was confined to an ~4-mm diameter around the catheter with this electrode design (see APPENDIX). The end-diastolic LV diameter is 7–9 mm in normal rats and 9–12 mm in rats with left heart failure (17). Because the interelectrode distance between the excitation electrodes was small enough to confine the current distribution volume to within the end-diastolic ventricular blood pool in the rat LV, we estimated ρ at end diastole (10, 28).

G_p was estimated by the dual-frequency excitation method (8, 9, 28) as follows

$$G_p = \kappa \times \Delta G_{20-2} \quad (2)$$

where ΔG_{20-2} is the difference in ventricular conductance values between the 20- and 2-kHz excitation frequencies and κ is an experimentally derived constant. Once κ is determined, G_p can be estimated from ΔG_{20-2}, obviating the need for saline infusion.

Instrumentation and Experimental Protocols

Thirty-three male Sprague-Dawley rats (350–400 g body wt) were used. Care of the animals was in strict accordance with the *Guiding Principles for the Care and Use of Animals in the Field of Physiological Sciences* as approved by the Physiological Society of Japan. The animals were anesthetized with pentobarbital sodium (50 mg/kg ip) and ventilated artificially. A vertical midline cervical incision was made to expose the right common carotid artery while the animal was in the supine position. The pressure-conductance catheter of the telemetry system was inserted into the LV retrogradely from the right common carotid artery. The position of the catheter was verified by monitoring the pressure-volume signal and by two-dimensional echocardiography. At the conclusion of the experiment, the animal was killed with an overdose of pentobarbital sodium, and the heart was examined to reconfirm the proper positioning of the catheter.

Group 1 (n = 23). We evaluated the accuracy of telemetric calibration of ρ and G_p under anesthetized, closed-chest conditions. Catheters (3-Fr) were inserted into the right and left jugular veins for blood sampling and saline injection, respectively. In 10 of the 23 rats, we compared ρ estimated telemetrically (ρ_{est}) with ρ measured from sampled blood by a conventional ex vivo cuvette method (ρ_{conv}). In the remaining 13 rats, we estimated G_p by the dual-frequency excitation method ($G_{p,est}$) and by the hypertonic saline method ($G_{p,conv}$). To obtain $G_{p,conv}$, we injected 20 μl of saturated saline into the right jugular vein while continuously measuring LV conductance (14, 23). To obtain $G_{p,est}$, we measured LV conductance at 2- and 20-kHz excitation frequencies and derived ΔG_{20-2} by averaging the instantaneous conductance difference over ~10 cardiac cycles. We randomly selected 7 of the 13 rats and determined the proportionality constant (κ in *Eq. 2*) from the averaged ratio of $G_{p,conv}$ to ΔG_{20-2}. $G_{p,est}$ and $G_{p,conv}$ were measured while the artificial ventilation was temporarily suspended at end expiration.

Group 2 (n = 4). Under anesthetized, open-chest conditions, we evaluated the accuracy of volumetry by comparing stroke volume (SV) measured by the telemetry system with SV measured by an ultrasonic flowmeter (model 2.5S273, Transonic Systems, Ithaca, NY). After median sternotomy, the aortic arch was dissected free from surrounding tissues. A flow probe was placed around the ascending aorta to measure the aortic blood flow. A string occluder was placed loosely around the inferior vena cava to decrease the LV preload and vary the SV over a wide range. We simultaneously measured the telemetric LV volume and the ultrasonic aortic blood flow while varying the preload. The measurements were done while the artificial ventilation was temporarily suspended at end expiration.

Group 3 (n = 6). Under conscious, closed-chest conditions, we evaluated the reproducibility of the telemetry on different days. Aseptic conditions were maintained throughout the surgical procedure. The telemetry system was implanted in a subcutaneous pocket made at the right upper dorsum. The skin was closed, and the animal was allowed to recover from anesthesia. On the day after implantation surgery, the LV volume, pressure, and an ECG were measured telemetrically in the fully recovered, conscious animal (*study 1*). Each rat underwent a second set of telemetric measurements at 1–6 days after the initial study (*study 2*). Ambient barometric pressure was measured simultaneously and subtracted from the telemetric LV pressure to compensate for changes in atmospheric pressure.

Data Collection

We used the real-time mode (200-Hz sampling) of the telemetry system and recorded LV conductance, LV pressure, intraventricular ECG, and ρ on a hard disk of a dedicated laboratory computer system (model HFPA031003, Epson, Tokyo, Japan). In *group 2*, ultrasonic aortic blood flow was digitized at 1,000 Hz through a 12-bit analog-to-digital converter and stored on a hard disk for subsequent analyses.

Statistical Analysis

For the calculation of LV volume using *Eq. 1*, *G* and ρ were obtained from the 20-kHz frequency component. In *group 1*, we used linear regression analysis to compare the telemetric and conventional measurements of ρ (ρ_{est} vs. ρ_{conv}) and G_p ($G_{p,est}$ vs. $G_{p,conv}$). In *group 2*, we calculated the telemetric SV from the difference between the end-diastolic volume (EDV) and end-systolic volume (ESV) in each beat. The flowmetric SV was computed from the time integral of aortic blood flow. The telemetric SV was compared with the flowmetric SV by linear regression analysis. In *group 3*, we compared heart rate (HR), EDV, ESV, end-diastolic pressure (EDP), and end-systolic pressure (ESP) between *study 1* and *study 2* for each rat. Using the pressure-volume data, we calculated ejection fraction (EF), maximal pressure increase ($+dP/dt_{max}$) or decrease ($-dP/dt_{max}$) over time, and the time constant of isovolumic relaxation (τ) and compared them between *study 1* and *study 2* for each rat. A nonparametric multiple comparison (Wilcoxon's signed-rank test) was used to examine the difference in each parameter between *study 1* and *study 2*. Group data are expressed as means (SD). Differences were considered significant at $P < 0.05$.

RESULTS

Telemetric Calibration of ρ

Figure 3*A* is a representative time series showing LV pressure and ρ at 2 and 20 kHz derived from the telemetry. The bottom of the ρ waveform, which corresponded to end diastole, represents the time when there was sufficient blood volume around the catheter (10). The lowest ρ values at 2 kHz ($\rho_{2\,kHz}$) and 20 kHz ($\rho_{20\,kHz}$) were very close (197 and 207 Ω·cm, respectively). This was the case for all the rats, indicating that ρ was frequency independent ($\rho_{2\,kHz} = 1.08\rho_{20\,kHz} - 13.8$, $r^2 = 0.96$, SE of the estimate = 6.7 Ω·cm) (6, 9). The lowest ρ at 20 kHz was treated as ρ_{est}.

Figure 3*B* summarizes the relation between ρ_{est} and ρ_{conv} obtained from 10 rats in *group 1*. ρ_{est} agreed with ρ_{conv} reasonably well ($\rho_{est} = 1.09\rho_{conv} - 11.9$, $r^2 = 0.88$, SE of the estimate = 10.7 Ω·cm). The ratio of SE of the estimate to the mean of ρ_{est} was 0.046, indicating small variability around the regression line.

Telemetric Calibration of G_p

Figure 4*A* illustrates a representative time series of telemetrically measured ECG, LV conductance signals at 2 and 20 kHz, and LV pressure. In this animal, ΔG_{20-2} was 0.56 mS

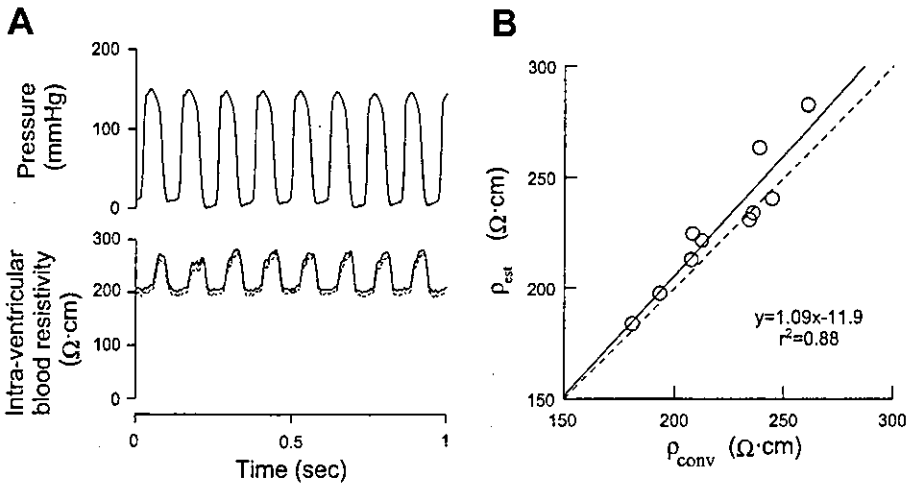

Fig. 3. *A*: waveforms of ventricular pressure and intraventricular blood resistivity at 2 kHz (dashed line) and 20 kHz (solid line) as a function of time obtained telemetrically. *B*: relation between blood resistivity as measured in a cuvette (ρ_{conv}) and as estimated via catheter electrodes (ρ_{est}) in 10 rats. Solid line, regression; dashed line, identity.

and $G_{p,conv}$ was 3.27 mS. Therefore, κ was calculated to be 5.79 from *Eq. 2* in this animal. The averaged κ from seven randomly selected rats was 5.14, which we used as the experimentally derived constant to obtain $G_{p,est}$ for all rats.

Figure 4*B* summarizes the relation between $G_{p,est}$ and $G_{p,conv}$ obtained from 13 rats in *group 1*. $G_{p,est}$ correlated well with $G_{p,conv}$ ($G_{p,est} = 1.59G_{p,conv} - 1.77$, $r^2 = 0.87$, SE of the estimate = 0.33 mS). The ratio of SE of the estimate to the mean of $G_{p,est}$ was 0.11, indicating that the estimation was reasonable around the mean of $G_{p,est}$.

Accuracy of the Televolumetry

Figure 5*A* depicts LV pressure and volume measured by telemetry and aortic blood flow measured by the ultrasonic flowmeter. Vena caval occlusion decreased LV pressure, volume, and aortic blood flow.

Figure 5*B* summarizes the relation between telemetric SV (SV_{tele}) and flowmetric SV (SV_{flow}) obtained from four rats in *group 2*. SV_{tele} matched SV_{flow} reasonably well in each of the four rats: $r^2 = 0.90-0.99$, slope = 0.86 (SD 0.16), intercept = 12.4 μl (SD 10.4), and SE of the estimate = 4.3 μl (SD 0.4). A linear regression analysis on the pooled data from all four rats also showed a highly linear relation between SV_{tele} and SV_{flow}: $SV_{tele} = 0.96SV_{flow} + 7.5$, $r^2 = 0.96$, SE of the estimate = 6.6 μl. The ratio of SE of the estimate to the mean of SV_{tele} was 0.10.

Reproducibility of the Telemetry

Individual data obtained by the telemetry system for all six rats in *group 3* are provided in Tables 1 and 2. The overall variability between repeated measurements in the same rat was reasonably small. There were no significant differences in repeated measurements of HR, EDV, ESV, EDP, and ESP between *study 1* and *study 2* (Table 1). There were no significant differences in repeated measurements of EF, $+dP/dt_{max}$, $-dP/dt_{max}$, and τ between *study 1* and *study 2* (Table 2).

Figure 6 illustrates the representative LV pressure-volume loops obtained from a rat in *group 3*. The pressure-volume loops in *studies 1* and *2* were almost identical.

DISCUSSION

We have developed a novel telemetry system for measurements of LV volume, pressure, and ECG in conscious, freely moving rats. The system, for the first time to the best of our knowledge, has enabled measurement of the LV pressure-

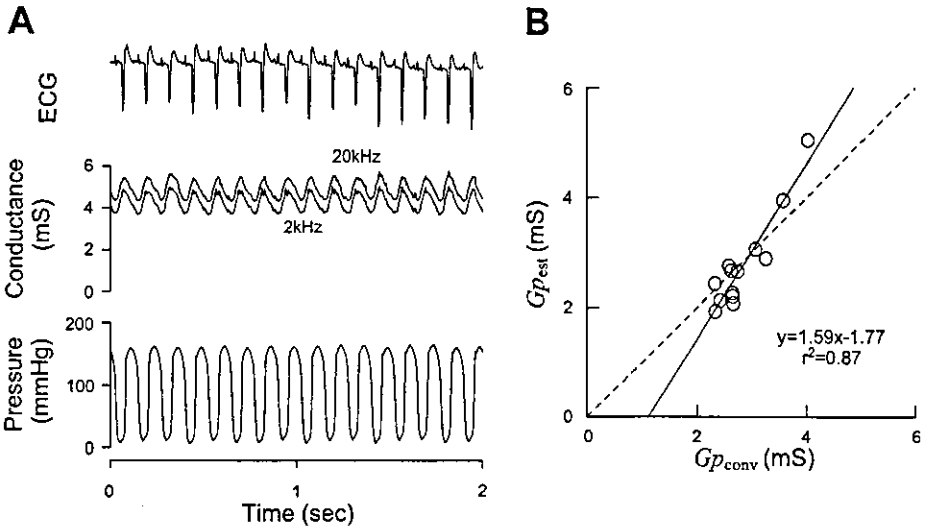

Fig. 4. *A*: waveforms of an ECG, conductance signals at 2 and 20 kHz, and ventricular pressure as a function of time, obtained telemetrically. *B*: relation between parallel conductance estimated by the saline infusion method ($G_{p,conv}$) and by dual-frequency excitation method ($G_{p,est}$) in 13 rats. Solid line, regression; dashed line, identity.

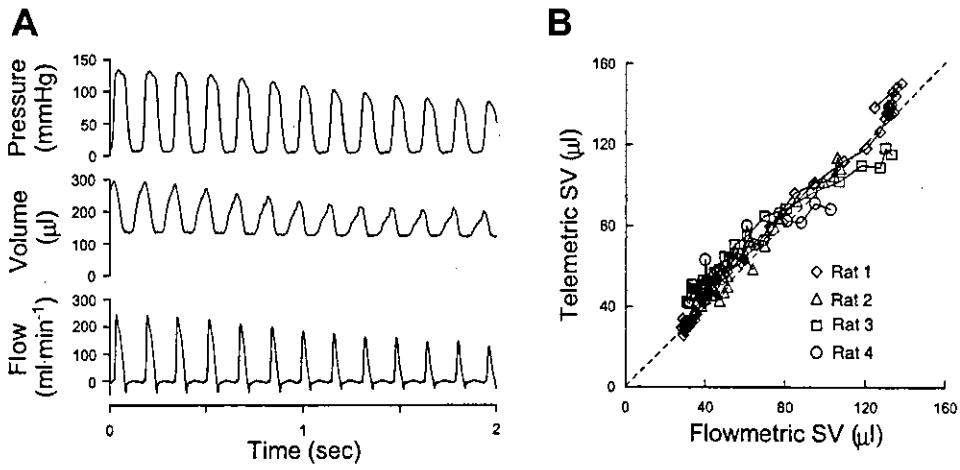

Fig. 5. *A*: representative traces of ventricular pressure, ventricular volume obtained telemetrically, and aortic flow measured by an ultrasonic flowmeter during vena cava occlusion in 1 rat. *B*: relation between telemetric stroke volume (SV) and flowmetric SV in 4 rats. Dashed line, identity.

volume relation in small experimental animals, such as rats, under completely conscious, unrestricted conditions with reasonably good accuracy and reproducibility.

Self-Calibrating Volumetry

In our conductance volumetric system, ρ and G_p were estimated using the telemetric signals alone (Figs. 3 and 4). We will be able to use the empirical constant κ (=5.14), determined in this study, in the future application of our telemetry system to rats. The self-calibrating feature made it possible to measure the LV pressure-volume relation in rats without tethering them for ex vivo calibration procedures, such as blood sampling and hypertonic saline infusion. Besides their impracticality in conscious, small animals, these procedures can alter hemodynamic conditions (6, 9). Frequent blood sampling can induce anemia. Concentrated saline injection depresses myocardial contractility and has volume-loading effects (6, 9). Our telemetry system is free of these problems.

The current used for resistivity measurements was distributed in a 2-mm radius around the catheter (see APPENDIX). The ratio of the radius (i.e., penetration depth) to the distance between the excitation electrodes was ~3 (≒2/0.6). This ratio is at odds with previously reported values, which were around or less than unity (6, 10, 26). Penetration depth is affected by the relation between the resistivity of the target tissue and that of the surrounding structure (26). This relation in our study was different from those in previous studies, which would be one reason for the discrepancy. Difference in shape and arrangement of the electrodes between our system and those previous studies would be another reason. Because the electrodes were placed very closely, stray capacitance between connecting wires could be a problem (31). The fact that resistivity values at 2 and 20 kHz were very close indicated that our titration method effectively removed the problem of stray capacitance (see APPENDIX). However, it might be better to incorporate techniques such as capacitance neutralization to completely prevent the problem, in case the capacitance were to significantly affect our titration accuracy in future long-term use, e.g., with increases in electrode impedance (31).

We used the dual-frequency excitation method previously described by Gawne et al. (8). Feldman et al. (6) combined measured resistivity of the myocardium with an analytic approach and estimated G_p from the conductance signals at 10 and 100 kHz. Although their method was completely independent of saline injection, it required measurement of myocardial resistivity with an additional four-electrode sensor.

Volumetric Accuracy and Reproducibility

We have verified the volumetric accuracy of our telemetry system by comparing SV_{tele} with SV_{flow} during inferior vena cava occlusions (Fig. 5*A*). The volumetric accuracy of the conductance catheter technique in the rat heart has been ex-

Table 1. *Reproducibility of hemodynamic variables*

	HR, beats/min		EDV, μl		ESV, μl		EDP, mmHg		ESP, mmHg	
Rat	S1	S2	S1	S2	S1	S2	S1	S2	S1	S2
1	530	475	303	307	168	182	14	19	131	123
2	363	476	310	280	212	151	11	17	121	133
3	426	500	330	355	212	220	12	9	127	129
4	405	511	244	194	143	89	14	13	120	125
5	402	382	364	434	269	326	15	14	119	106
6	400	380	240	283	158	167	24	36	142	152
Mean (SD)	421 (57.3)	454 (58.2)	299 (49)	309 (81)	194 (47)	189 (80)	15 (5)	18 (10)	127 (9)	128 (15)
Difference										
Mean (SD)	65 (40)		37 (23)		34 (26)		5 (4)		8 (4)	
Percent difference										
Mean (SD)	15 (9)		13 (8)		20 (17)		28 (16)		6 (4)	

S1, *study 1;* S2, *study 2;* HR, heart rate; EDV, left ventricular end-diastolic volume; ESV, left ventricular end-systolic volume; EDP, left ventricular end-diastolic pressure; ESP, left ventricular end-systolic pressure.

Table 2. *Reproducibility of parameters of ventricular functions*

Rat	EF, %		+dP/dt$_{max}$, mmHg/s		−dP/dt$_{max}$, mmHg/s		τ, ms	
	S1	S2	S1	S2	S1	S2	S1	S2
1	45	41	10,594	9,615	7,165	6,648	9.2	9.0
2	32	46	9,284	11,802	6,364	7,372	8.5	8.3
3	36	38	10,373	12,129	7,277	6,937	9.4	8.1
4	42	54	9,274	11,801	7,527	7,013	6.4	9.5
5	26	25	8,862	7,610	6,132	4,878	7.4	7.9
6	34	41	9,808	9,756	7,518	7,273	11.0	12.4
Mean (SD)	36 (7)	41 (10)	9,699 (682)	10,452 (1,773)	6,997 (601)	6,687 (923)	8.7 (1.6)	9.2 (1.7)
Difference								
Mean (SD)	7 (5)		1513 (957)		646 (397)		1.1 (1.1)	
Percent difference								
Mean (SD)	17 (13)		15 (9)		10 (7)		13 (14)	

EF, left ventricular ejection fraction; dP/dt$_{max}$, maximal pressure rise (+) or decrease (−) over time; τ, time constant of isovolumic left ventricular relaxation.

amined using a similar comparison (14, 23). Ito et al. (14) reported a very high and linear correlation (r = 0.97–0.99) between conductance-derived SV and SV measured by an electromagnetic flowmeter in rats. We also obtained a similar highly linear relation between SV_{tele} and SV_{flow} (Fig. 5*B*).

The reproducibility of our telemetry system (Table 1) is good enough for many applications, such as the study of LV remodeling in rats. This is because EDV has been reported to increase to ~200% of the control value in rats with ischemic heart failure and in heart failure-prone rats (2, 7, 12).

Applications of the Telemetry System

The developed telemetry system enables detailed evaluation of cardiac function in small animals by eliminating the effects of anesthesia and acute surgical intervention (13, 22, 30). By using a single-beat estimation method to determine the ESPVR, our system would enable evaluation of the load-independent contractile index in conscious animals (24, 25). We validated pressure-volume signals only under control conditions in this study. The stability of the acquired data and the capacity of our system to monitor altered hemodynamics remain to be evaluated.

Our telemetry system is potentially useful for the long-term monitoring of LV function. We confirmed that our system was viable for up to 8 days in this study. However, further studies are required to definitively evaluate the longevity of the implants over a longer period of time (19). Thrombosis and infection would affect the morbidity and mortality associated with the chronic implantation of our system. Coating of the pressure-conductance catheter with anticoagulants and further miniaturization of the implant are under development to ameliorate such problems.

We adopted Bluetooth technology for telecommunication. Bluetooth is a wireless technology designed to allow low-cost, short-range radio links between mobile personal computers and other portable devices (18). While point-to-point connections are supported, Bluetooth technology allows up to seven simultaneous connections to be established and maintained by a single receiver (18). This unique feature of Bluetooth technology should be beneficial in experimental settings where a large population of animals in a single cage must be evaluated (16).

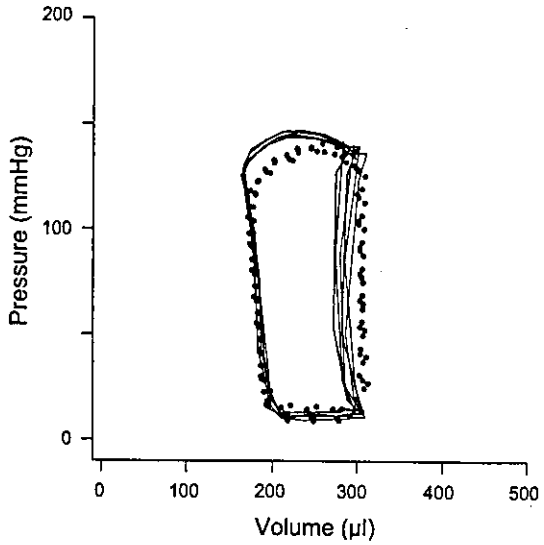

Fig. 6. Day-to-day reproducibility of LV pressure-volume loops in 1 rat. Thick solid loops, *study 1*; dotted loops, *study 2*. Loops for *studies 1* and *2* (6 days apart) were superimposable.

Limitations

The volume calibration factor α was assumed to be unity on the basis of the preliminary experiment, where the conductance-derived volume was close to true syringe volume in the normal operating range for rats (Fig. 2). Georgakopoulos and Kass (9) noted that the relation was quite linear when the volume range was limited to the physiological operating range for mice. Hettrick et al. (11) also noted that conductance-derived volume was close to true syringe volume and α was unity in a volume range. However, both groups and others noted that the relation was nonlinear when considered over a wider volume range (1, 9, 11, 20). In addition, the syringes have no G_p, whereas the rat heart does. It has been shown that G_p has significant effects on α (11). Taken together, these findings suggest that it will be necessary to recalibrate α when we apply our system to the rat LV in heart failure or other cardiac disorders, where drastic changes in ventricular volume and changes in the electrical properties of surrounding structures, i.e., change in G_p, are probable (1).

Values of EF in Table 2 are low for normal rats (5, 7). Other parameters of LV function are, however, within the normal

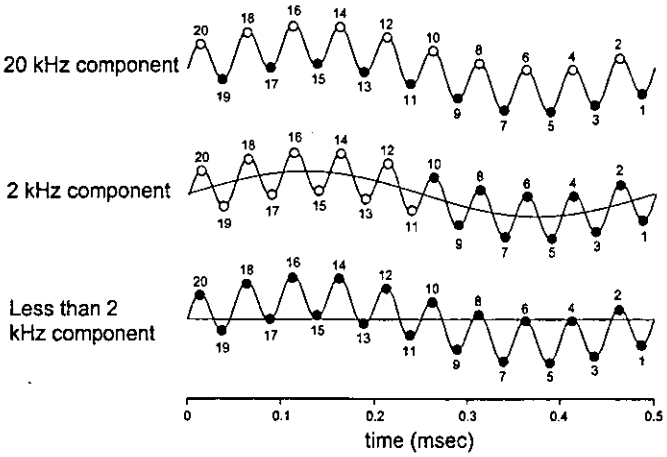

Fig. 7. Visual representation of logical processing used to extract 20-, 2-, and <2-kHz frequency components of digital signals.

range (5, 7) (Table 2). Dual-frequency derived G_p values from the rats in *group 3* ranged from 1.8 to 3.3 mS (mean 2.3 ± 0.4 mS). The dual-frequency method slightly underestimated G_p in that range compared with the saline injection method (Fig. 4*B*). This might result in an apparent reduction of EF. To settle the discrepancy between EF and other functional parameters, it is necessary to compare the telemetric EF with the EF determined by other independent methods, such as echocardiography.

We were able to estimate ρ in the LV cavity in normal-sized rats with the present catheter design (Fig. 1*B*, *inset*). However, the catheter design may not be applicable to smaller rats or mice, where the current distribution volume probably distributes outside the LV cavity. To apply our system to these small animals, further reduction of the interelectrode distance is required for measurement of ρ.

Conclusion

A novel telemetry system was developed for measurements of LV pressure, volume, and ECG in conscious, freely moving rats. The system enabled us to accurately measure the LV pressure-volume relation with good reproducibility and without the harmful effects of anesthesia or acute surgical trauma in rats.

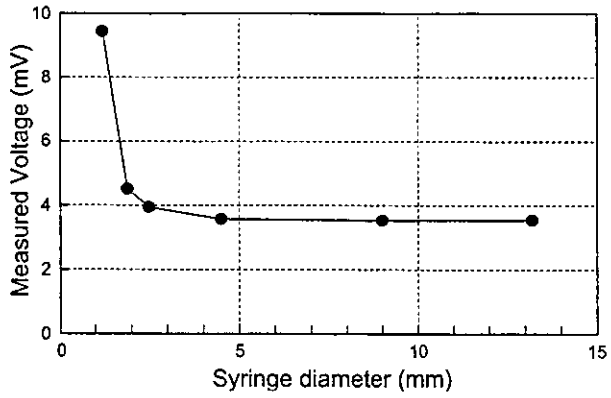

Fig. 8. Relation between syringe diameter and voltage as measured by sensing electrodes of our conductance catheter designed for blood resistivity measurement. Voltage reaches a minimum at a syringe diameter of ~4 mm. This indicates that current distribution volume is confined to within a 4-mm diameter around the catheter.

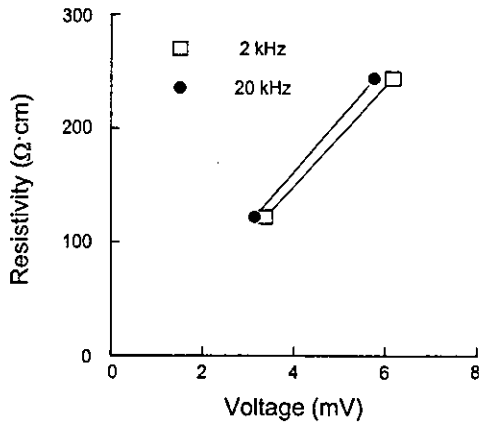

Fig. 9. Relation between measured voltage and saline resistivity.

APPENDIX

Logical processing of digital signals to extract frequency components. We extracted frequency components of 20 kHz, 2 kHz, and low frequency (<2 kHz) by logical processing of digital signals. The analog signals were converted to digital signals at a sampling rate of 40 kHz. Twenty serial digital values were processed simultaneously (Fig. 7). We obtained the 20-kHz component on the basis of the difference between even- and odd-numbered digital values. We calculated an average of every 10 digital values. We obtained the 2-kHz component on the basis of the difference between the two averaged values of the former half and the latter half (average of 10 values each). We obtained the low-frequency component by averaging all 20 digital values. All this logical processing was performed by the programmable logic device (Fig. 1*C*).

Estimation of intraventricular ρ. First, we experimentally determined the current distribution volume of the four small electrodes for estimation of ρ. We placed our pressure-conductance catheter at the center of plastic syringes of various sizes filled with diluted saline. Saline resistivity was matched to that of the blood (122 Ω·cm). We injected a constant current (20 kHz, 20 μA RMS) into the excitation electrodes (0.6 mm apart; Fig. 1*B*, *inset*) and measured voltage via the sensing electrodes. We present the relation between the measured voltage and the syringe diameter in Fig. 8. As demonstrated, with increasing syringe diameter, the voltage signal decreased and reached a minimum at a syringe diameter of ~4 mm. This implied that most (>95%) of the current was confined to within the cylindrical diameter at which the voltage reached a minimum. From these data, we concluded that the current distribution volume was confined to within a 4-mm diameter around the catheter.

Second, the resultant voltage signal was converted to ρ by a conversion formula. We determined the conversion formula experimentally by placing the catheter at the center of a plastic syringe with a diameter of 9 mm. Syringes were filled with diluted saline solutions with known resistivities in the range of those expected in rat blood (122 and 244 Ω·cm). Constant currents (20 and 2 kHz, 20 μA RMS) were injected between the excitation electrodes. We linearly related the measured RMS voltage to saline resistivity and used this relation as a conversion formula (Fig. 9).

ACKNOWLEDGMENTS

This study was presented in part at the Scientific Sessions of the American Heart Association, Orlando, FL, November 2003.

GRANTS

This study was supported by Ministry of Health Labour and Welfare of Japan Health and Labour Sciences Research Grants for Research on Advanced Medical Technology 13090401 and H14-Nano-002 and Japan Society for the Promotion of Science Grants-in-Aid for Scientific Research A 15200040, C

14570707, and C 15590786, by a Ground-Based Research Grant for space utilization promoted by the National Space Development Agency of Japan and the Japan Space Forum, and by the Program for Promotion of Fundamental Studies in Health Science of the Organization for Pharmaceutical Safety and Research of Japan.

REFERENCES

1. **Applegate RJ, Cheng CP, and Little WC.** Simultaneous conductance catheter and dimension assessment of left ventricle volume in the intact animal. *Circulation* 81: 638–648, 1990.
2. **Asanoi H, Ishizaka S, Kameyama T, Nozawa T, Miyagi K, and Sasayama S.** Serial reproducibility of conductance catheter volumetry of left ventricle in conscious dogs. *Am J Physiol Heart Circ Physiol* 262: H911–H915, 1992.
3. **Baan J, Jong TT, Kerkhof PL, Moene RJ, van Dijk AD, van der Velde ET, and Koops J.** Continuous stroke volume and cardiac output from intra-ventricular dimensions obtained with impedance catheter. *Cardiovasc Res* 15: 328–334, 1981.
4. **Baan J, van der Velde ET, de Bruin HG, Smeenk GJ, Koops J, van Dijk AD, Temmerman D, Senden J, and Buis B.** Continuous measurement of left ventricular volume in animals and humans by conductance catheter. *Circulation* 70: 812–823, 1984.
5. **Cingolani OH, Yang XP, Cavasin MA, and Carretero OA.** Increased systolic performance with diastolic dysfunction in adult spontaneously hypertensive rats. *Hypertension* 41: 249–254, 2003.
6. **Feldman MD, Mao Y, Valvano JW, Pearce JA, and Freeman GL.** Development of a multifrequency conductance catheter-based system to determine LV function in mice. *Am J Physiol Heart Circ Physiol* 279: H1411–H1420, 2000.
7. **Francis J, Weiss RM, Wei SG, Johnson AK, and Felder RB.** Progression of heart failure after myocardial infarction in the rat. *Am J Physiol Regul Integr Comp Physiol* 281: R1734–R1745, 2001.
8. **Gawne TJ, Gray KS, and Goldstein RE.** Estimating left ventricular offset volume using dual-frequency conductance catheters. *J Appl Physiol* 63: 872–876, 1987.
9. **Georgakopoulos D and Kass DA.** Estimation of parallel conductance by dual-frequency conductance catheter in mice. *Am J Physiol Heart Circ Physiol* 279: H443–H450, 2000.
10. **Gopakumaran B, Osborn P, Petre JH, and Murray PA.** A new technique to measure and track blood resistivity in intracardiac impedance volumetry. *J Clin Monit* 13: 363–371, 1997.
11. **Hettrick DA, Battocletti JH, Ackmann JJ, Linehan JH, and Warltier DC.** Effects of physical parameters on the cylindrical model for volume measurement by conductance. *Ann Biomed Eng* 25: 126–134, 1997.
12. **Heyen JR, Blasi ER, Nikula K, Rocha R, Daust HA, Frierdich G, Van Vleet JF, De Ciechi P, McMahon EG, and Rudolph AE.** Structural, functional, and molecular characterization of the SHHF model of heart failure. *Am J Physiol Heart Circ Physiol* 283: H1775–H1784, 2002.
13. **Hoit BD, Ball N, and Walsh RA.** Invasive hemodynamics and force-frequency relationships in open- versus closed-chest mice. *Am J Physiol Heart Circ Physiol* 273: H2528–H2533, 1997.
14. **Ito H, Takaki M, Yamaguchi H, Tachibana H, and Suga H.** Left ventricular volumetric conductance catheter for rats. *Am J Physiol Heart Circ Physiol* 270: H1509–H1514, 1996.
15. **Kubota T, Mahler CM, McTiernan CF, Wu CC, Feldman MD, and Feldman AM.** End-systolic pressure-dimension relationship of in situ mouse left ventricle. *J Mol Cell Cardiol* 30: 357–363, 1998.
16. **Lapointe N, Blais C Jr, Adam A, Parker T, Sirois MG, Gosselin H, Clement R, and Rouleau JL.** Comparison of the effects of an angiotensin-converting enzyme inhibitor and a vasopeptidase inhibitor after myocardial infarction in the rat. *J Am Coll Cardiol* 39: 1692–1698, 2002.
17. **Litwin SE, Katz SE, Morgan JP, and Douglas PS.** Serial echocardiographic assessment of left ventricular geometry and function after large myocardial infarction in the rat. *Circulation* 89: 345–354, 1994.
18. **Lou E, Fedorak MV, Hill DL, Raso JV, Moreau MJ, and Mahood JK.** Bluetooth wireless database for scoliosis clinics. *Med Biol Eng Comput* 41: 346–349, 2003.
19. **Mills PA, Huetteman DA, Brockway BP, Zwiers LM, Gelsema AJ, Schwartz RS, and Kramer K.** A new method for measurement of blood pressure, heart rate, and activity in the mouse by radiotelemetry. *J Appl Physiol* 88: 1537–1544, 2000.
20. **Mur G and Baan J.** Computation of the input impedances of a catheter for cardiac volumetry. *IEEE Trans Biomed Eng* 31: 448–453, 1984.
21. **Murphy AM, Kogler H, Georgakopoulos D, McDonough JL, Kass DA, Van Eyk JE, and Marban E.** Transgenic mouse model of stunned myocardium. *Science* 287: 488–491, 2000.
22. **Price HL and Ohnishi ST.** Effects of anesthetics on the heart. *Fed Proc* 39: 1575–1579, 1980.
23. **Sato T, Shishido T, Kawada T, Miyano H, Miyashita H, Inagaki M, Sugimachi M, and Sunagawa K.** ESPVR of in situ rat left ventricle shows contractility-dependent curvilinearity. *Am J Physiol Heart Circ Physiol* 274: H1429–H1434, 1998.
24. **Sato T, Shishido T, Miyashita H, Yoshimura R, and Sunagawa K.** Single-beat estimation of end-systolic elastance (E_{es}) in rats (Abstract). *Circulation* 96 *Suppl* I: I-518, 1997.
25. **Shishido T, Hayashi K, Shigemi K, Sato T, Sugimachi M, and Sunagawa K.** Single-beat estimation of end-systolic elastance using bilinearly approximated time-varying elastance curve. *Circulation* 102: 1983–1989, 2000.
26. **Steendijk P, Mur G, Van Der Velde ET, and Baan J.** The four-electrode resistivity technique in anisotropic media: theoretical analysis and application on myocardial tissue in vivo. *IEEE Trans Biomed Eng* 40: 1138–1148, 1993.
27. **Uechi M, Asai K, Osaka M, Smith A, Sato N, Wagner TE, Ishikawa Y, Hayakawa H, Vatner DE, Shannon RP, Homcy CJ, and Vatner SF.** Depressed heart rate variability and arterial baroreflex in conscious transgenic mice with overexpression of cardiac $G_s\alpha$. *Circ Res* 82: 416–423, 1998.
28. **Uemura K, Sugimachi M, Shishido T, Kawada T, Inagaki M, Zheng C, Sato T, and Sunagawa K.** Convenient automated conductance volumetric system. *Jpn J Physiol* 52: 497–503, 2002.
29. **Uemura K, Sugimachi M, and Sunagawa K.** Self-calibratable ventricular pressure-volume telemetry system for rats (Abstract). *Circulation* 108 *Suppl* IV: IV-37, 2003.
30. **Vatner SF and Braunwald E.** Cardiovascular control mechanisms in the conscious state. *N Engl J Med* 293: 970–976, 1975.
31. **Wood JW.** Stray-capacitance neutralisation for high-resistance microelectrodes—a simple analysis. *Med Biol Eng Comput* 19: 230–236, 1981.

Annals of Biomedical Engineering, Vol. 32, No. 10, October 2004 (© 2004) pp. 1365–1383

Adaptive Predictive Control of Arterial Blood Pressure Based on a Neural Network during Acute Hypotension

KOJI KASHIHARA,[1,2] TORU KAWADA,[1] KAZUNORI UEMURA,[1] MASARU SUGIMACHI,[1] and KENJI SUNAGAWA[1]

[1]Department of Cardiovascular Dynamics, National Cardiovascular Center Research Institute, 5-7-1 Fujishirodai, Suita, Osaka 565-8565, Japan and [2]The Organization for Pharmaceutical Safety and Research, Shin-Kasumigaseki Building, 3-3-2 Kasumigaseki, Chiyoda, Tokyo 100-0013, Japan

(Received 7 August 2003; accepted 20 May 2004)

Abstract—In acute hypotension, an automated drug infusion system to control mean arterial blood pressure (MAP) has not been previously studied, though many investigations have examined the use of vasodilating drugs to control MAP in postoperative hypertension. Therefore, we examined an automated control of MAP during acute hypotension using a neural network (NN) approach. A proportional-integral-derivative (PID) control, an adaptive predictive control using a NN (APC_{NN}), a combined control of APC_{NN} and PID ($APC_{NN\text{-}PID}$), a fuzzy control, and a model predictive control were tested in computer simulation based on the MAP response to norepinephrine (NE) of 25 $\mu g\ ml^{-1}$. In six anesthetized rabbits, using the NE of 25 $\mu g\ ml^{-1}$, the PID control, APC_{NN}, and $APC_{NN\text{-}PID}$ prevented severe hypotension compared to an uncontrolled condition. Under PID control, four of the six animals showed MAP oscillation. Using NE of 50 $\mu g\ ml^{-1}$, the rabbits recovered from acute hypotension for all systems tested but showed sustained MAP oscillation during PID control. In conclusion, utilization of a NN for adaptive predictive control systems could facilitate the development of an automated drug infusion apparatus because it provides robust control even when acute or large perturbations and inter-individual differences in the sensitivity to therapeutic agents occur.

Keywords—Automated drug infusion system, Norepinephrine, Rabbits, Proportional-integral-derivative control.

INTRODUCTION

In a clinical setting, it is necessary to regulate many physiological parameters in the presence of disturbances including interactions among therapeutic agents, unexpected and acute changes in hemodynamic variables, and background noise.[9] Many investigators have reported on the use of automated drug infusion systems using vasodilators in postoperative hypertension[13,18,28] and multiple drug infusion systems to regulate hemodynamics such as cardiac output and mean arterial blood pressure (MAP).[9,22] However, in acute hypotension, an automated drug infusion system to control MAP has not been studied previously because no controller was robust enough to handle the associated unexpected large disturbances and complex modeling of various pathological states. If a system could be designed, which adapted to acute hypotension, and combined with a multiple drug infusion system,[9,22] it would be useful for application in a clinical setting.

Catecholamines, fluid infusion, and blood transfusion are required to maintain local circulation to vital organs during acute hypotension.[3,6,26] The catecholamines contribute to the quick recovery of MAP from a state of acute hypotension.[20,31] However, the sensitivity or responsiveness to the pharmacological agents generally differs among patients, and even within the same individual, the effects of pharmacological intervention could vary with time due to changes in a patient's underlying pathophysiology.[2] Further, the dose-response relationship is usually nonlinear, which makes a prediction of MAP response difficult. The cumulative effects of the past intervention on the current MAP[29] also complicate MAP control. Therefore, proper drug infusion for MAP control largely relies on the expertise of anesthesiologists and clinicians. Developing a reliable method for automating the drug infusion system would improve a patient's individualized drug therapy and minimize the total amount of drug required, which may allow an early tapering off of the drug.

Automated drug infusion systems for controlling MAP have been constructed previously using proportional-integral-derivative (PID) algorithms.[19,27] As long as the MAP response to pharmacological intervention does not change markedly, simple control with PID-tuned parameters works reasonably well. However, the PID controller cannot achieve maximum performance in all situations because of the nonlinear time-varying MAP response and the differences of drug sensitivity among patients.[1,13,34] To overcome the limitation of PID control, adaptive MAP controls have been developed to provide consistent

Address correspondence to Koji Kashihara, Department of Cardiovascular Dynamics, National Cardiovascular Center Research Institute, 5-7-1 Fujishirodai, Suita, Osaka 565-8565, Japan. Electronic mail: kasihara@ri.ncvc.go.jp

0090-6964/04/1000-1365/1

performance. These adaptive controllers recursively update their own parameters so as to compensate for both the time-varying characteristics of MAP response and the intra- and inter-individual differences to drug sensitivity.[18,28,33] Because the conventional adaptive controls still rely on a moment-to-moment linearity in MAP response to drug infusion, they might not be able to adapt to the nonlinear MAP response when large perturbations such as acute and severe hypotension[1] occur.

A neural network (NN) is a useful tool that can identify and learn nonlinear time-varying systems even in the presence of intra- and inter-individual variability in a patient's vital signs with large perturbations.[15,30] Therefore, an adaptive predictive control based on a NN (APC_{NN}) may be more robust compared to the conventional PID controller in stabilizing the system in the presence of nonlinearities in patient response and sensitivities to a drug.[1,11,17] The purpose of the present study was to explore the utility of a MAP control system based on an APC_{NN} algorithm. One limitation of using an advanced algorithm is that the added computational expense results in longer times for system identification compared to a simpler algorithm such as PID control. To overcome this performance limitation, we also constructed an APC_{NN} combined with PID control ($APC_{NN\text{-}PID}$). The performance of the APC_{NN} and $APC_{NN\text{-}PID}$ systems was compared to that of a traditional PID system, using a hemorrhage-induced acute hypotension condition to alter MAP. To estimate the effects of the simple adaptive control using artificial intelligence or the predictive control compared with APC_{NN} or $APC_{NN\text{-}PID}$, we tested the PID control based on fuzzy inference or model predictive control (MPC). Finally, we tested the robustness of each system, to control MAP, using two different concentrations of a vasopressor agent, norepinephrine (NE), at concentrations of 25 and 50 μg ml^{-1}.

METHODS

Modeling of MAP Response

To make a simple model for MAP response to a drug infusion, we obtained the average step response as MAP changed from baseline (ΔMAP) during a 5-min NE infusion at 3 μg kg^{-1} min^{-1} in anesthetized rabbits ($n = 3$) without hemorrhage [Fig. 1(a)]. The ΔMAP response (sampling rate = 10 Hz) was averaged every 10 s. We approximated the step response of ΔMAP to the following first-order delay system with a pure time delay:

$$\Delta\mathrm{MAP}(t) = \begin{cases} K \cdot \left[1 - \exp\left(-\dfrac{t-L}{T}\right)\right] & (t \geq L) \\ 0 & (t < L) \end{cases} \quad (1)$$

where K is a proportional gain [mmHg (μg kg^{-1} min^{-1})$^{-1}$], T is a time constant (s), and L is the pure time delay (s).

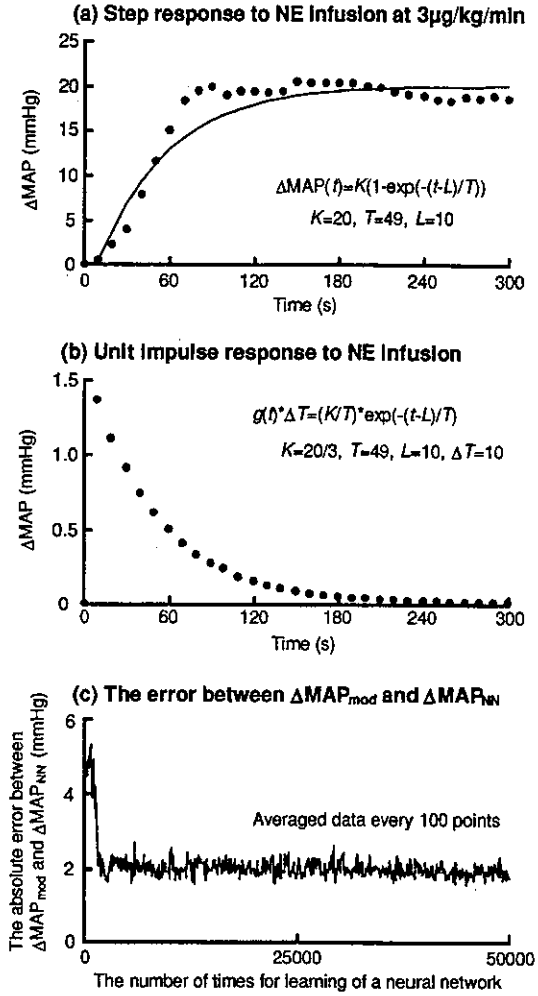

FIGURE 1. (a) Step response to norepinephrine (NE) infusion at 3 μg kg^{-1} min^{-1}, (b) Unit impulse response to NE infusion, (c) The absolute error between actual changes in mean arterial blood pressure (ΔMAP(t)) as the model ($\Delta MAP_{mod}(t)$) and $\Delta MAP_{NN}(t)$ showing predicted changes in MAP by a neural network (NN).

$K = 20$, $T = 49$, and $L = 10$ were acquired from the approximation of the averaged step response [Fig. 1(a)].

The ΔMAP response as a model (ΔMAP_{mod}) was calculated by the convolution integral in the discrete-time domain as follows:

$$\Delta\mathrm{MAP}_{\mathrm{mod}}(t) = \sum_{\tau=0}^{N_m} g(\tau) \cdot \Delta T \cdot u(t-\tau) \quad (2)$$

where

$$g(t) = \frac{K}{T} \cdot \exp\left(-\frac{t-L}{T}\right)$$

$u(t)$ is the infusion rate of NE (μg kg^{-1} min^{-1}) and $g(t)$ is the unit impulse response (mmHg). The $g(t)$ is calculated from the derivative values of the step response of Eq. (1) [Fig. 1(b)]. ΔT is the sampling interval (s) and N_m is the finite number of terms in the model for the unit impulse response.

K is a proportional gain [mmHg (μg kg^{-1} min^{-1})$^{-1}$], T is a time constant (s), and L is the pure time delay (s). The parameters of ΔMAP_{mod} were $\Delta T = 10$, $N_m = 30$, $K = 20/3$, $T = 49$, and $L = 10$.

Design of Controllers

PID Control

We applied the PID algorithm as a velocity form algorithm. The velocity form algorithm determines the drug infusion rate rather than the total amount of drug infused. The algorithm can be expressed in the discrete time domain as follows [Fig. 2(a)],[4]

$$\Delta u(t) = K_P \cdot \left\{ [e(t) - e(t-1)] + \frac{\Delta T}{T_I} \cdot e(t) + \frac{T_D}{\Delta T} \cdot [e(t) - 2 \cdot e(t-1) + e(t-2)] \right\} \quad (3)$$

$$u(t) = u(t-1) + \Delta u(t)$$

where $u(t)$ = NE infusion rate (μg kg^{-1} min^{-1}), $\Delta u(t)$ = change in $u(t)$, K_P = proportional gain [(μg kg^{-1} min^{-1}) mmHg^{-1}], T_I = integral time (s), T_D = derivative time (s), ΔT = sampling interval (10 s), $e(t)$ = difference (mmHg) between a target value and observed MAP at a given time. PID parameters were determined by the Ziegler–Nichols[36] method, resulting in $K_P = 0.3$, $T_I = 20$, and $T_D = 5$.

Adaptive Predictive Control Based on a NN (APC_{NN})

Figure 2(b) shows a block diagram of an APC_{NN} system. The APC_{NN} is a control system where the NN shown in Fig. 3 recursively learns the characteristics of a patient using their observed ΔMAP response to NE infusion, and then determines the predicted output after N_p steps. First, in the closed loop controls, the NN learned about ΔMAP response only once every 10 s to prevent overlearning of ΔMAP during rapid disturbances or artifacts ["1. Learning Loop" in Fig. 2(b) and (c)]. Second, the learned ΔMAP_{NN} response was used for the prediction of future ΔMAP responses by the NN ["2. Prediction Loop" in Fig. 2(b) and (c)]. The initial connection weights for the NN were determined from the learning-stage results using the ΔMAP_{mod} [see Eq. (2)].

Feed-Forward Output Using a NN. Figure 3 shows the components of a NN. A multilayer feed-forward NN with two hidden layers was used to emulate the ΔMAP_{mod} response. The NN structure used was a nonlinear autoregressive moving average (NARMA) model[1,32] as follows:

$$\Delta MAP_{NN}(t) = f(\Delta MAP(t-1), u(t-1), u(t-2), u(t-3), u(t-4), u(t-5), u(t-6)) \quad (4)$$

where $\Delta MAP_{NN}(t)$ is the MAP change estimated by the NN. $\Delta MAP(t-1)$ is the actual MAP change induced by NE infusion before one sampling interval (10 s) has passed. The input layer in a NN is composed of the past input and output. The duration of past NE infusion rate was set to 1 min accounting for the pure time delay in the ΔMAP response differing among patients.

The input values are sent through the first hidden layer, second hidden layer, and output layer (see Feed-Forward Output Using a NN under Appendix). When the NN calculates the output, the hyperbolic tangent function is applied 14 times (7 in the first hidden layer and 7 in the second hidden layer).

Backpropagation Algorithm for Learning. To identify the MAP response and determine the initial weights in a NN for MAP controls, the NN was trained using the output of the ΔMAP_{mod} response to random inputs. In the present study, we used the backpropagation algorithm in the online mode as follows.

All connection weights are adjusted to decrease the error function by the backpropagation learning rule based on the gradient descent method.[24,25] The error function, E is as follows:

$$E = \frac{1}{2} \cdot \varepsilon^2 = \frac{1}{2} \cdot [\Delta MAP - \Delta MAP_{NN}]^2 \quad (5)$$

where ΔMAP is the actual MAP change as a supervised signal, ΔMAP_{NN} is the ΔMAP predicted by the NN before update of the connection weights, and ε is the difference between ΔMAP and ΔMAP_{NN}. The ΔMAP_{NN} predicted by a NN is compared with the actual ΔMAP, and its error is calculated by Eq. (5). The error is back propagated through the network, and the connection weight is generally updated by the gradient descent of E as a function of the weights.[30]

$$w^* = w + Kn \cdot \Delta w \quad (6)$$

where

$$\Delta w = \frac{\partial E}{\partial w} = \frac{\partial E}{\partial \varepsilon} \cdot \frac{\partial \varepsilon}{\partial MAP_{NN}} \cdot \frac{\partial MAP_{NN}}{\partial w} = -\varepsilon \cdot \frac{\partial MAP_{NN}}{\partial w},$$

w^* is the weight of each connection after update, w is the weight of each connection before update, Δw is the modified weight, K_n is the learning rate.

In the present study, the backpropagation algorithm was performed in the following order: output layer, second hidden layer, and first hidden layer (see Backpropagation Algorithm for Learning under Appendix). The total number of weights in the NN was 120 (105 for layer weights and 15 for bias, Fig. 3). The combination of a fixed input $x_0 = 1$ and an extra input weight w_0 is known as a bias input (Fig. 3[1,30]).

Determination of Initial Weights in a NN. To determine the initial weights in the NN for the APC_{NN} and $APC_{NN\text{-}PID}$, we made the NN learn the ΔMAP_{mod} response. The starting